1 **A Synthesis of Global Streamflow characteristics, Hydrometeorology, and**

2 **catchment Attributes (GSHA) for Large Sample River-Centric Studies**

4 Ziyun Yin[1], Peirong Lin[1,2*], Ryan Riggs[3], George H. Allen[4], Xiangyong Lei[1], Ziyan

5 Zheng[5,6], Siyu Cai[7]

6 1. Institute of Remote Sensing and GIS, School of Earth and Space Sciences, Peking University

7 2. International Research Center for Big Data for Sustainable Development Goals, Beijing, China

8 3. Department of Geography, Texas A&M University, Texas, USA

9 4. Department of Geosciences, Virginia Polytechnic Institute and State University, Virginia, USA

10 5. Key Laboratory of Regional Climate-Environment Research for Temperate East Asia, Institute of

11   Atmospheric Physics, Chinese Academy of Sciences, Beijing, China

12 6. University of Chinese Academy of Sciences, Beijing, China

13 7. State Key Laboratory of Simulation and Regulation of Water Cycle in River Basin, China Institute

14   of Water Resources and Hydropower Research, Beijing, China

15 * *Correspondence to*: Peirong Lin (peironglinlin@pku.edu.cn)

Abstract

17   Our understanding and predictive capability of streamflow processes largely rely on high-
18 quality datasets that depict a river's upstream basin characteristics. Recent proliferation of large
19 sample hydrology (LSH) datasets has promoted model parameter estimation and data-driven
20 analyses of the hydrological processes worldwide, yet existing LSH is still insufficient in terms of
21 sample coverage, uncertainty estimates, and dynamic descriptions of anthropogenic activities. To
22 bridge the gap, we contribute the Synthesis of Global Streamflow characteristics, Hydrometeorology,
23 and catchment Attributes (GSHA) to complement existing LSH datasets, which covers 21,568
24 watersheds from 13 agencies for as long as 43 years based on discharge observations scraped from
25 web. In addition to annual and monthly streamflow indices, each basin's daily meteorological
26 variables (i.e., precipitation, 2 m air temperature, longwave/shortwave radiation, wind speed, actual
27 and potential evapotranspiration), daily-weekly water storage terms (i.e., snow water equivalence,
28 soil moisture, groundwater percentage), and yearly dynamic descriptors of the land surface
29 characteristics (i.e., urban/cropland/forest fractions, leaf area index, reservoir storage and degree of
30 regulation) are also provided by combining openly available remote sensing and reanalysis datasets.
31 The uncertainties of all meteorological variables are estimated with independent data sources. Our
32 analyses reveal the following insights: (i) the meteorological data uncertainties vary across variables
33 and geographical regions, which should be accounted for by LSH users, (ii) ~6% watersheds shifted
34 between human managed and natural states during 2001-2015 including those with environmental
35 recovery projects in Northeast China, which may inform hydrologic analysis that takes the changing
36 land surface characteristics into account, and (iii) GSHA watersheds showed a more widespread
37 declining trend in runoff coefficient than an increasing trend, pointing to critical water availability
38 issues. Overall, GSHA is expected to serve hydrological model parameter estimation and data-
39 driven analyses as it continues to improve. GSHA v1.1 can be accessed at
40 *https://doi.org/10.5281/zenodo.8090704* and *https://doi.org/10.5281/zenodo. 10433905* . (Yin et al.,

41   2023).

1 Introduction

43   Climate change has posed profound challenges to the management of freshwater resources,
44   specifically riverine floods or water shortages (AghaKouchak et al., 2020; Thackeray et al., 2022).
45   The urgent need for flood and drought forecasting, water resources planning and management, all
46   call for high-quality streamflow predictions for basins worldwide to analyse global terrestrial water
47   conditions in a systematic view (Burges, 1998). The scarcity of hydrological observations has
48   brought challenges to these predictions (Belvederesi et al., 2022; Hrachowitz et al., 2013), thus the
49   development of computer models that allow for "modelling everything everywhere" (Beven &
50   Alcock, 2012) constitutes the backbone of hydrological studies. Existing studies have used
51   physically-based and data-driven models for streamflow simulation (Lin et al., 2018; Nandi &
52   Reddy, 2022; Zhang et al., 2020), with efforts to improve accuracy of prediction by combining both
53   (Cho & Kim, 2022; Razavi & Coulibaly, 2013). Yet the prediction of the magnitude, timing, and
54   trend of critical streamflow characteristics are still subject to multiple sources of errors and
55   uncertainties (Bourdin et al., 2012; Brunner et al., 2021).
56   Streamflow (Q) can be represented by the simple water balance equation involving
57   precipitation (P), evapotranspiration (ET), and water storage terms (S) denoted as $Q = P - ET - \Delta S$,
58   yet influencing factors of these components could bring uncertainties that cascade downstream.
59   Starting from the model assumptions to the data used to represent climate, soil water, ice cover,
60   topography and land use, as well as the less well-known processes such as human perturbations and
61   sub-surface flows (Benke et al., 2008; Wilby & Dessai, 2010), these complications impede our
62   understanding of streamflow processes across scales, which also limits the modelling and predictive
63   capability for streamflow. Thus, reducing the predictive uncertainties requires high-quality data with
64   massive samples capable of depicting each of the water balance components, as well as the natural
65   and anthropogenic factors involved (Gupta et al., 2014).
66   Efforts have been made to address the need for such kind of high-quality datasets on watershed-
67   scale hydro-climate and environmental conditions during the past couple of decades. One of the
68   earliest was the most widely used dataset generated for the Model Parameter Estimation Experiment
69   (MOPEX) project aimed at better hydrological modelling (Duan et al., 2006). Historical hydro-
70   meteorological data and land surface characteristics for over 400 hydrologic basins in the United
71   States were provided, which was fundamental to the progress in large sample hydrology (LSH)
72   (Addor et al., 2020; Schaake et al., 2006). Later the dataset was expanded to 671 catchments in the
73   contiguous United States (CONUS) and benchmarked by model results (Newman et al., 2015).
74   Based on these studies, the Catchment Attributes and Meteorology for Large-sample Studies
75   (CAMELS) dataset was developed, providing comprehensive and updated data on topography,
76   climate, streamflow, land cover, soil, and geology attributes for each catchment (Addor et al., 2017).
77   The CONUS CAMELS dataset soon became influential in LSH and has since inspired researchers
78   from Australia (Fowler et al., 2021), Europe (Coxon et al., 2020; Delaigue et al., 2022; Klingler et
79   al., 2021), South America (Alvarez-Garreton et al., 2018; Chagas et al., 2020), and China (Hao et

al., 2021) to contribute their regional CAMELS. Another comprehensive regional LSH dataset for North America named the Hydrometeorological Sandbox - École de Technologies Supérieure (HYSETS) dataset, was also developed with larger sample size (14425 watersheds) and richer data sources compared with the CAMELS (Arsenault et al., 2020).

While these datasets are reliable data sources for regional studies, attempts on building global datasets have become the new norm in the era of big data to boost our analytical and modelling capability for the terrestrial hydrological processes. The HydroATLAS dataset integrated indices of hydrology, physiography, climate, land cover, soil, geology, and anthropogenic activity attributes for 8.5 million global river reaches (Lehner et al., 2022; Linke et al., 2019). A recent work combined a series of CAMELS datasets with HydroATLAS attributes into a new global community dataset on the cloud named Caravan, with dynamic hydro-climate variables and comprehensive static catchment attributes extracted on 6830 watersheds (Kratzert et al., 2023), which represents by far the most comprehensive synthesis of existing CAMELS. Another global-scale effort, the Global Streamflow Indices and Metadata archive (GSIM), incorporated dynamic streamflow indices and attribute metadata for topography, climate type, land cover, etc., for over 35000 gauges (Do et al., 2018; Gudmundsson et al., 2018), and the streamflow indices were updated to allow for trend analysis (Chen et al., 2023). A recent study filled in the discontinuity and latency of gauge records, and provided streamflow for over 45,000 gauges with improved data quality (Riggs et al., 2023). These global-scale datasets have been widely used in data-driven machine learning models (Kratzert et al., 2019a, 2019b; Ren et al., 2020), physical hydrological models (Aerts et al., 2022; Clark et al., 2021), and parameter estimation and regionalization studies (Addor et al., 2018; Fang et al., 2022).

Although the flourishment of LSH datasets has promoted comparative hydrological studies (Kovács, 1984) and large-scale hydrological modeling and analysis efforts, several challenges are still standing in the way of realizing the full potential of LSH. As briefly outlined in a recent review by Addor et al. (2020), current LSH datasets lack common standards, metadata and uncertainty estimates, and are insufficient in characterising human interventions. More specifically, the following major critical aspects still need attention from the LSH developers, which we attempt to address with GSHA (Yin et al., 2023). First, the majority of current datasets (especially those at a global scale) incorporated only one data source for each variable, while earth observations, reanalysis, satellite-based estimates are subject to uncertainties (Merchant et al., 2017; Ukhurebor et al., 2020). These uncertainties were rarely represented and may bring difficulties to the regionalization of model parameters (Beck et al., 2016), while also resulting in inconsistent conclusions. Second, anthropogenic activities including land use and land cover (LULC) changes, dam and reservoir building, etc., are critical drivers of shifts in streamflow statistical moments (Niraula et al., 2015). However, historical time series of watershed human modifications were rarely included in LSH datasets, which is particularly problematic for regions with rapid economic growth. Finally, although the most recent Caravan provided hydroclimate data for global watersheds, the samples are limited to the existing regional CAMELS which Caravan synthesizes. Therefore, plenty of room is left to increase data sample size and spatial coverage by revisiting the streamflow data acquisition process in a more comprehensive way.

To complement existing LSH datasets, we contribute the first version of a synthesis of Global Streamflow characteristics, Hydrometeorology, and catchment Attributes (GSHA v_1.0) for large-sample river-centric studies. GSHA features the following characteristics:

- Updated physical and anthropogenic descriptors of global rivers, covering streamflow

124   characteristics, hydrometeorological variables, and land use land cover changes for 21568
125   watersheds derived from gauged streamflow records from 13 agencies.
126   ● Streamflow indices for data scarce regions, including those derived from 263 gauges in
127   China, are included.
128   ● Extended temporal coverage for as long as 43 years (1979-2021), which varies regionally.
129   ● Uncertainty estimates for the meteorological variables.
130   ● Dynamic descriptors for the urban, forest, and cropland fractions, as well as reservoir
131   storage capacity to improve the representation of human activities in the basin.

132   With the above features, we expect GSHA to support hydrological model parameter estimation
133   and data-driven analysis of global streamflow as one of the most comprehensive LSH datasets
134   regarding sample size, variable dynamics, and uncertainty estimates. **Table 1** summarizes the
135   differences between GSHA and other prominent LSH datasets. Our paper is organized as follows.
136   Section 2 expands on **Table 1** and provides more details of the data included for GSHA. Section 3
137   introduces the data sources and methodologies involved in creating GSHA. Section 4 highlights the
138   key features of GSHA by conducting some analyses, followed by conclusions reached in Section 5.
139

140   **Table 1 Comparison of GSHA with other LSH datasets.** Note that we only include the CONUS
141   CAMELS dataset to represent regional LSH datasets for this comparison, as other regional CAMELS
142   share large similarity with CONUS CAMELS.

Factors	CAMELS (eg. US)	HydroATLAS	Caravan	GSIM	GSHA
Spatial extent	Regional	Global	Global	Global	Global
Sample size	671	8.5 million	6830	35002	21568
Time span	1980–2015	Static	1981–2020	1806-2016	1979-2021
Streamflow dynamics	Yes	No	Yes	Yes (statistical indices)	Yes (monthly and yearly statistical indices)
Meteorological time series	Yes	No	Yes	No	Yes
Multi data sources for meteorological variables	Yes	No	No	No	Yes (**with uncertainty estimates**)
Water storage dynamics	No	No	Only soil water dynamics	No	**Yes**
Land cover dynamics	No	No	No	No	**Yes**
Reservoir dynamics	No	No	No	No	**Yes**
Static attributes	Yes	Yes	Yes (from HydroATLAS)	Yes	Yes (from HydroATLAS)

2 Dataset content of GSHA v1

In this section, the data fields, variables, and attributes included in GSHA are described in more details and summarized in **Table 2**. For the instructions of the data format, we provide a user manual along with the dataset (see readme.docx). GSHA includes yearly and monthly streamflow characteristics derived from daily discharge observations, meteorological variables (including precipitation, 2-m air temperature, long- and shortwave radiation, wind speed, actual and potential evapotranspiration (AET and PET)), daily or weekly water storage terms (4 layers of soil moisture, groundwater, and snow depth water equivalence), daily vegetation index (leaf area index (LAI)), yearly LULC characteristics (urban, cropland, and forest fraction), and yearly reservoir information (degree of regulation (DOR) and reservoir capacity). For each meteorological variable, multiple independent data sources are incorporated to provide uncertainty estimates. Static attributes like land physiography, soils, and geology are not additionally extracted, as similar efforts have been made by other researchers, so we directly matched our gauge locations to the HydroATLAS dataset (Lehner et al., 2022; Linke et al., 2019) by providing the river ID match table. Users can link the two to obtain these attributes.

Watershed polygons: GSHA includes 21568 watershed polygons delineated from the global gauges, which are stored as Esri Shapefile format. The ID and agency of each watershed is the same as the corresponding gauge ID, and the gauge latitude/longitude are in decimal degree. The area denotes the upstream drainage area of the gauge. Some of the IDs contain characters (such as '.', '-', etc.) inconsistent with the majority of IDs. For the convenience of the users, we unified these as underscores and stored the new file names as 'filename'. We also provide independent files summarizing basic information of the watersheds, including matched MERIT river reach COMID, upstream area, order and downstream river reach COMID, as well as verification with officially reported areas of the agencies.

Streamflow indices: GSHA publishes annual and monthly streamflow indices derived from daily streamflow data, including different percentiles, and mean/median/minimum/maximum. The frequency and durations of extremely high and low streamflow events are also provided. We also include numbers of zero observations and valid samples to allow flexible data screening by the users. The indices are stored as comma-separated values (CSV) files, with each watershed corresponding to one file. A complementary R package can be used to automatically download many of the gauge datasets is available at https://github.com/Ryan-Riggs/RivRetrieve (Riggs et al., 2023).

Meteorological variables: The meteorological variables selected are the most influential drivers for streamflow, which include precipitation, 2-m temperature, ET, radiation and wind speed. In main-stream land surface models, ET is a diagnostic variable derived from meteorological inputs and is not considered as meteorological forcing. However, as many hydrological models also use potential ET as an input variable, and model calibration sometimes involves actual ET (Immerzeel & Droogers, 2008), we include the two variables and place them into the meteorological variable category. For each variable, more than one data sources are used to allow for uncertainty analysis, which is provided on a yearly basis in an independent file.

182   **Natural water storage terms and land use/land cover change:** These include soil moisture,
183   snow water equivalent, and groundwater percentages. We also include yearly land cover dynamics
184   (i.e., urban, forest, and cropland fraction changes), as well as dynamically changing reservoir
185   capacity and degree of regulation (DOR) percentage. Leaf area index (LAI) is also included to
186   reflect the seasonal changes in vegetation canopy that are also key to the streamflow processes.

187   **Static attributes:** GSHA does not extract updated static attributes because HydroATLAS
188   already made substantial efforts in this regard. Instead, the listed categories are those mostly related
189   to streamflow prediction from HydroATLAS selected to be included in GSHA files, and we direct
190   the readers to the ID match table to access the entire 281 static attributes offered by HydroATLAS
191   (Lehner et al., 2022; Linke et al., 2019). Our user manual, available at the dataset download site,
192   also provides more information on it.

193

194   **Table 2 Fields provided with GSHA.**

Category	Field	Description	Unit
Watershed Polygons and basic information	Sttn_Nm	The ID of the watershed.	NaN
	Latitude	Latitude of the gauge.	Degree
	Longitude	Longitude of the gauge.	Degree
	Shedarea	The area of delineated watershed.	Km^2
	Agency	The agency the gauge belongs to.	NaN
	filename	The name of the corresponding Shapefile in the dataset.	NaN
	verification	Verification of watershed area with officially reported area of the corresponding agency. If we did not access the officially reported area of the watershed on the agency website, the field would be "unverified".	NaN
	COMID	ID of the MERIT river reach matching with the watershed.	NaN
	uparea	Upstream area of the river reach included in the MERIT database.	NaN
	order	Stream order of the river reach.	NaN
	NextDownID	ID of the downstream river reach in MERIT.	NaN

Category	Indices	Description	Unit/Format
Streamflow indices (yearly)	percentiles	Annual 1, 10, 25, 75, 90, 99 percentiles of daily streamflow.	m^3/s
	mean	Annual mean of daily streamflow.	m^3/s
	median	Annual median of daily streamflow.	m^3/s
	annual maximum flood (AMF)	Annual maximum of daily streamflow.	m^3/s
	AMF occurrence date	The date of AMF occurrence.	Year/month/day

	frequency of high-flow events	Number of days in a year with streamflow >= 90 percentile flow.	Days/year
	average duration of high-flow events	Average number of consecutive days >= 90 percentile flow.	Days
	frequency of low-flow events	Number of days in a year with streamflow <= 10 percentile flow.	Days/year
	average duration of low-flow events	Average number of consecutive days <= 10 percentile flow.	Days
	Q=0 days	Number of days with runoff=0.	Days
	valid observation days	Number of days with no missing data. (Valid observations refer to non-null measurements.)	Days
	month with nan>10 days	A list of the months with over 10 days of NaN measurement.	Month

Category	Indices	Description	Unit/Format
Streamflow indices (monthly)	percentiles	Monthly 1, 10, 25, 75, 90, 99 percentiles of daily streamflow.	m^3/s
	mean	Monthly mean of daily streamflow.	m^3/s
	median	Monthly median of daily streamflow.	m^3/s
	monthly maximum flood (MMF)	Monthly maximum of daily streamflow.	m^3/s
	MMF occurrence date	The date of MMF occurrence.	Year/month/day
	frequency of high-flow events	Number of days in a month with streamflow >= yearly 90 percentile flow.	Days/month
	average duration of high-flow events	Average number of consecutive days in the month >= yearly 90 percentile flow.	Days
	frequency of low-flow events	Number of days in a month with streamflow <= yearly 10 percentile flow.	Days/month
	average duration of low-flow events	Average number of consecutive days in the month <= yearly 10 percentile flow.	Days
	Q=0 days	Number of days with runoff=0.	Days
	valid observation days	Number of days with no missing data.	Days

Category	Variable	Data source name	Unit
Meteorological Variables	Precipitation	MSWEP	mm
		EM-Earth	mm
	2 m temperature	ERA5	K
		MERRA-2	K
		EUSTACE	K
	Actual evapotranspiration	REA	mm
		GLEAM	mm

	Potential	GLEAM	mm
	evapotranspiration	hPET	mm
	Radiation (longwave)	ERA5 land surface net thermal radiation	W/m^2
		MERRA-2 surface net downward longwave flux	W/m^2
	Radiation (shortwave)	ERA5 land surface net solar radiation	W/m^2
		MERRA-2 surface net downward shortwave flux	W/m^2
	10 m wind speed (u component)	ERA5 land u-component of wind	m/s
		MERRA-2 10 metre eastward wind	m/s
	10 m wind speed (v component)	ERA5 land v-component of wind	m/s
		MERRA-2 10 metre northward wind	m/s
	10 m wind speed (actual)	ERA5 land u- and v-components of wind	m/s
		MERRA-2 10 metre northward and eastward wind	m/s

Category	**Variable**	**Data source name**	**Unit**
Water storage terms	Soil moisture layer 1	ERA5 land soil water layer 1 (0-7 cm, 0cm refers to the surface)	m^3/m^3
	Soil moisture layer 2	ERA5 land soil water layer 2 (7-28 cm)	m^3/m^3
	Soil moisture layer 3	ERA5 land soil water layer 3 (28-100 cm)	m^3/m^3
	Soil moisture layer 4	ERA5 land soil water layer 4 (100-289 cm)	m^3/m^3
	Snow water equivalent	ERA5 land snow depth water equivalent	m of water equivalent
	Ground water	GRACE-FO data assimilation	%

Category	**Variable**	**Data source name**	**Unit**
Land use and land cover	Urban fraction	GAUD	%
	Forest fraction	MCD12Q1	%
	Cropland fraction	MCD12Q1	%
	Reservoir capacity	GeoDAR	Million m^3
	DOR	GeoDAR	%
	LAI	CDR LAI	NaN

Category	**Attribute**	**Column name (directly from RiverATLAS)**	**Unit**
Static-Physiography	Elevation	ele_mt_uav	m. a.s.l.
	Terrain slope	slp_dg_uav	degrees (x10)
	Stream gradient	sgr_dk_rav	decimetres per km
Static-Hydrology	Inundation Extent	inu_pc_ult	%
	Groundwater Table	gwt_cm_cav	cm

	Depth		
Static-Landcover	Land Cover Classes	glc_cl_cmj	NaN
	Potential Natural Vegetation Classes	pnv_cl_cmj	NaN
	Wetland Extent	wet_pc_u01-u09	%
	Glacier Extent	gla_pc_use	%
	Permafrost Extent	prm_pc_use	%
Static-Soil & geology	Clay Fraction in Soil	cly_pc_uav	%
	Silt Fraction in Soil	slt_pc_uav	%
	Sand Fraction in Soil	snd_pc_uav	%
	Lithological Classes	lit_cl_cmj	NaN
	Soil Erosion	ero_kh_uav	kg/hectare per year

3 Data sources and methodology

3.1 Technical workflow in creating GSHA

The creation of GSHA starts from revisiting the data compilation process for the stream gauging observations from 13 international agencies. The general workflow of GSHA data production processes is illustrated in **Figure 1**, which consists of watershed delineation, variable extraction from both grid and non-grid data sources, and uncertainty analysis.

First, we delineated the upstream watersheds using gauge locations. Calibration of gauge longitudes and latitudes were conducted to match the gauges with the MERIT river network exactly. The delineated watersheds were selected and manually checked using standards of area, topology correctness, and observation data lengths. The selected watersheds went on to be overlayed with grid and non-grid variable data sources for to obtain GSHA variables.
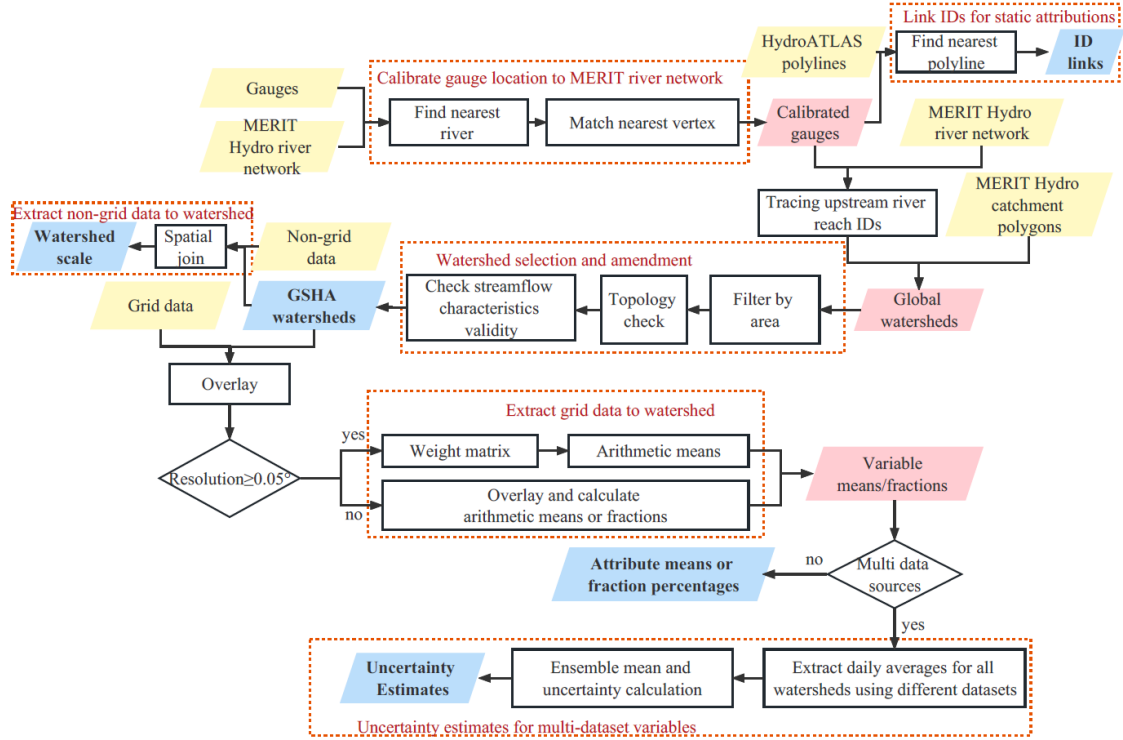
206
207 **Figure 1 General workflow of GSHA.** The yellow parallelograms are the input datasets, the blue ones
208 are the final outputs of GSHA dataset, and the pink ones are the results in the process. The black
209 quadrilaterals represent the extraction and calculation processes, and the red dotted rectangles illustrate
210 different modules of the extraction process.

3.2 Gauge-based streamflow indices

212 As shown in **Table 3**, in total streamflow data from 36497 gauges were initially scraped from
213 the web and from the Chinese National Real-time Rain and Water Situation Database. For gauges
214 located within ~100 m of each other, those with fewer years of measurements were removed,
215 assuming that they are redundant with one another. The gauge measurements were converted to a
216 consistent unit (m^3/s) and then manually compared with GRDC measurements to ensure accurate
217 unit conversion (Riggs et al., 2023). Gauge databases compiled in this study are available through
218 a variety of web interfaces, except for the Chinese Hydrology Project (CHP) data which is provided
219 by the authors of the dataset (Henck et al 2010, Schmidt et al 2011), and processed into annual scale
220 data that meets the requirements of the synthesis dataset.

Table 3 Gauge data sources used in this analysis. N1 and N2 refers to numbers of gauges with observations after 1979 and used in GSHA. The starting and ending years (Y1 and Y2) of GSHA gauges for each agency are listed.

Source	N1	N2	Y1	Y2	URL/Provider
ArcticNET 2022	116	106	1979	2003	www.r-arcticnet.sr.unh.edu/v4.0/AllData/index.html
Australian Bureau of Meteorology 2022 (BOM)	4017	2340	1979	2021	www.bom.gov.au/waterdata/
Brazil National Water Agency 2022 (ANA)	1343	1172	1979	2021	www.snirh.gov.br/hidroweb/serieshistoricas
Canada National Water Data Archive 2022 (HYDAT)	3771	2222	1979	2021	www.canada.ca/en/environment-climate-change/services/water-overview/quantity/monitoring/survey/data-products-services/national-
Chile Center for Climate and Resilience Research 2022(CCRR)	481	392	1979	2020	https://explorador.cr2.cl/
Chinese Hydrology Project (CHP)	112	26	1979	1987	(Henck et al 2010, Schmidt et al 2011)
The Global Runoff Data Centre 2022 (GRDC)	6345	4004	1979	2021	(https://portal.grdc.bafg.de/applications/public.html?publicuser=PublicUser
India Water Resources Information System 2022 (IWRIS)	547	261	1979	2020	https://indiawris.gov.in/wris/#/RiverMonitoring
Japanese Water Information System 2022 (MLIT)	1023	751	1979	2019	www1.river.go.jp/
Spain Annuario de Aforos, 2022 (AFD)	1138	889	1979	2018	http://datos.gob.es/es/catalogo/e00125801-anuario-de-aforos/resource/48368826-e7fd-4a41-950c-89b4eaea0279
Thailand Royal Irrigation Department 2022 (RID)	126	73	1980	1999	http://hydro.iis.u-tokyo.ac.jp/GAME-T/GAIN-T/routine/rid-river/disc_d.html
U.S. Geological Survey 2022 (USGS)	16951	9069	1979	2021	https://waterdata.usgs.gov/nwis/rt
Chinese National Real-time Rain and Water Situation Database	527	263	2000	2019	http://xxfb.mwr.cn/sq_zdysq.html

221 ## 3.3 Watershed delineation

222   The watershed delineation process was built upon a vector-based global river network dataset
223 (Lin et al., 2021), which is delineated from the 90-m Multi-Error-Removed Improved Terrain
224 (MERIT) digital elevation model (DEM) (Yamazaki et al., 2017) and the flow direction and flow
225 accumulation rasters (Yamazaki et al., 2019). The locations of the gauges may contain locational
226 errors and direct delineation will result into erroneous watershed boundaries; therefore, gauge
227 location correction was conducted by relocating the gauges to the nearest MERIT-based river reach
228 vertices. The adjusted gauge points were used as the watershed outlets, where the contributing areas
229 were extracted by dissolving all upstream catchments based on the topology provided by MERIT
230 Basins (Lin et al., 2019). Since the area threshold of MERIT Basins is 25 km^2, we did not include
231 watersheds smaller than this threshold. Considering the spatial heterogeneity of very large basins,
232 we excluded watersheds ≥50,000 km^2 from the dataset. To ensure GSHA supports studies with
233 sufficiently long records, only watersheds with >5 years of observations since 1979 were selected.
234 For gauges sharing the same watershed, the one with better data quality (i.e., longer measurement
235 records and more valid observation days) was used. If the two gauges share the same quality, we
236 only included the furthest downstream gauge. Eventually, the selection processes resulted in 21568
237 valid watersheds out of 35970 gauges initially scraped from the web plus 527 gauges from the
238 Chinese National Real-time Rain and Water Situation Database (**Figure 2**).
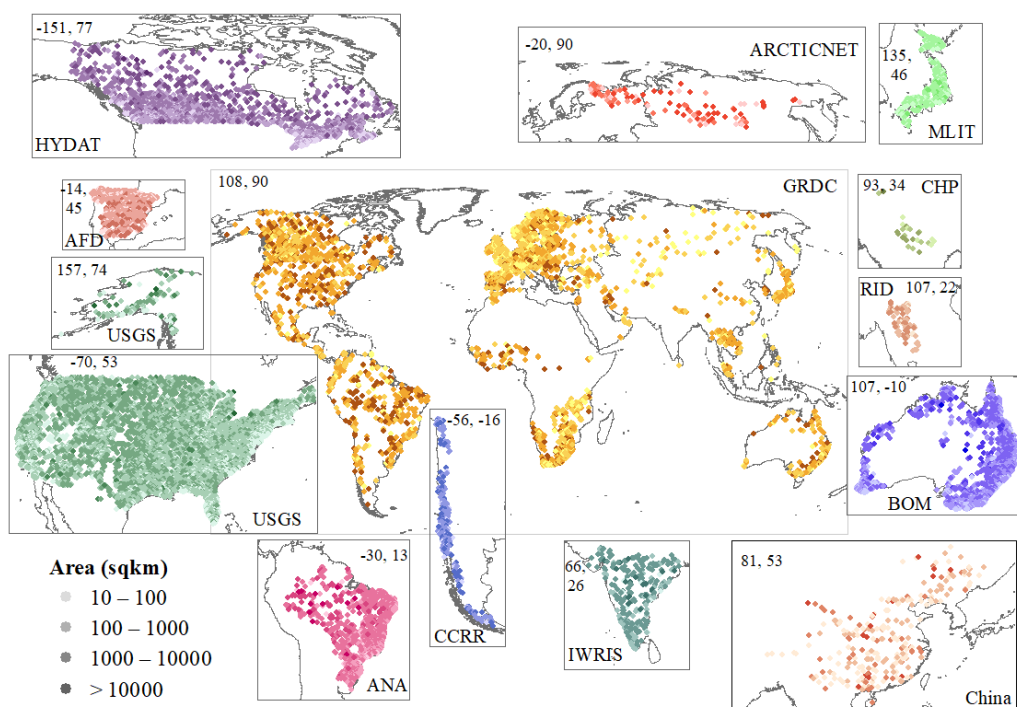
240 **Figure 2 Spatial distribution of the GSHA gauges (n=21568).** Watershed areas are represented by the
241 tint of colours. Gauges of different agencies are represented with separate colours and are plotted in
242 individual frames (except for USGS gauges in two frames to incorporate Alaska). The agency names and
243 the upper-left coordinates (longitude, latitude) of each frame are also shown in the figure.

244

245   The GSHA watersheds are unevenly distributed across the globe, more than half of which are
246 located in North America (USGS, HYDAT, and a large proportion of GRDC gauges, **Figure 3a**).

Europe, Australia, and South America also have relatively good coverage, while Asia and Africa
show the lowest gauge densities. The majority of the gauged watersheds are of medium sizes ranging
from 250 to 2500 km^2, although for some agencies it does not show the same distribution (**Figure
3d**). For instance, ANA (South America), IWRIS (India), and arcticnet (Northern Eurasia)
watersheds are generally larger, while the Chinese National Real-time Rain and Water Situation
Database provides more gauges with smaller drainage areas. Due to the maintenance difficulties,
the number of functioning gauges is declining for agencies like GRDC, but the lack of data in recent
years (**Figure 3c**) is mainly due to latency issues. USGS, BOM, and ANA provide a stable number
of observations for the 1980-2021 period (**Figure 3c**) with high proportions of valid observations
each year (**Figure 3b**), while observational periods from arcticnet and China contain relatively fewer
valid samples (**Figure 3b**) and shorter time spans (**Figure 3c**).
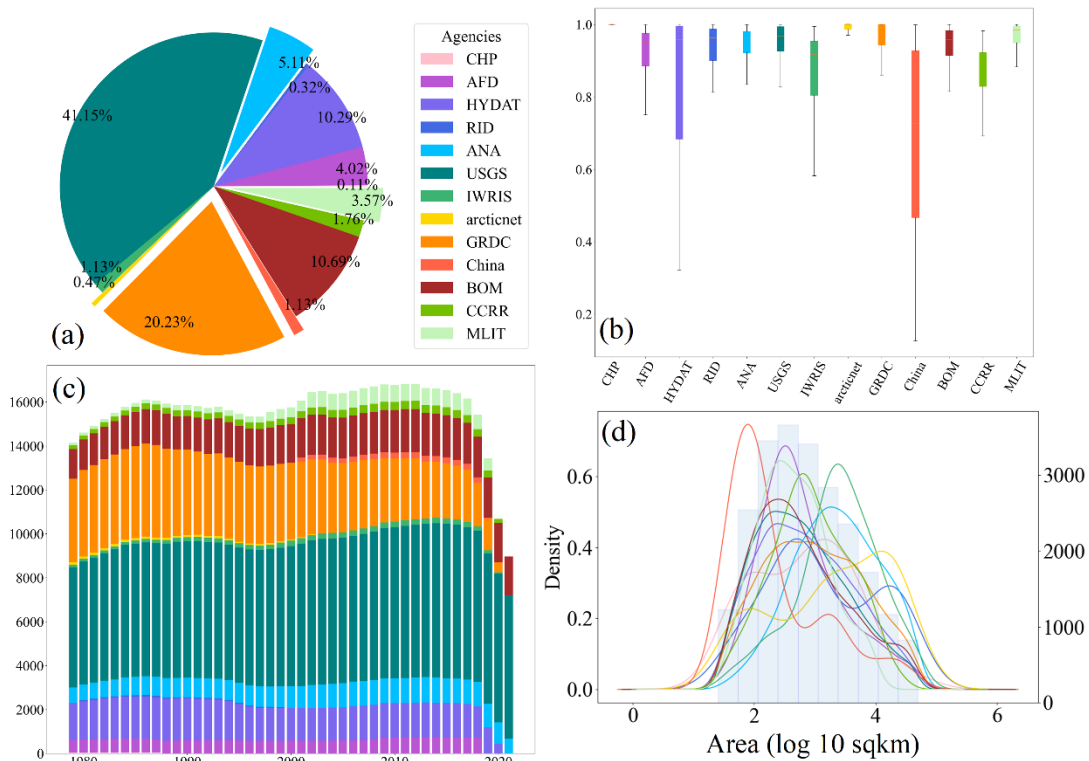
Figure 3 Summary statistics of the GSHA gauges. This includes (a) proportions of gauges from
different agencies, (b) box plots for proportions of valid observations for each agency, (c) proportion of
valid observation for each year by agency and (d) distributions of watershed areas for each agency
(kernel density estimation lines, left y-axis) and all gauges (blue histogram, right y-axis). The colour
legend in subplot (a) applies to all four subplots. In subfigure (a) the 0.11% label corresponds to CHP,
and the legend goes counter clockwise in the pie chart. In subfigure (c), CHP bars are at the bottom of
the plot, and the legend goes from bottom to the top of the bars.

3.4 Meteorological variables, water storage terms, and land surface characteristics

After watershed delineation, publicly available grid or non-grid data were obtained and
overlaid to derive the meteorological, water storage terms, and land surface characteristics. The data
sources used for GSHA are listed in **Table 4**. We prioritized the use of multi-source fusion datasets

270   with relatively high quality surveyed from literature when creating GSHA.

271   3.4.1 Meteorology datasets

272   For precipitation, the Multi-Source Weighted-Ensemble Precipitation (MSWEP) that merged
273   gauge measurements (CPC Unified), grid data (GPCC), satellite products (CMORPH, GSMaP-
274   MVK, and TMPA 3B42RT), and reanalysis data (ERA-Interim and JRA-55) with sample density
275   and comparative performance considered (Beck et al., 2017; Beck et al., 2019) are included. Another
276   precipitation dataset is the Ensemble Meteorological Dataset for Planet Earth (EM-Earth)
277   deterministic estimates, which merged a station-based Serially Complete Earth (SC-Earth)
278   removing the temporal discontinuities in raw station observations and ERA5 estimates (Tang et al.,
279   2022).
280   For 2-m air temperature, the EUSTACE global land station daily air temperature dataset
281   (EUSTACE) statistically merged station and satellite observations to obtain global daily near-
282   surface air temperature (Brugnara et al., 2019) is included. Other datasets used for 2-m temperature
283   extraction are the reanalysis datasets Modern-Era Retrospective analysis for Research and
284   Applications Version 2 (MERRA-2) (Gelaro et al., 2017) and the fifth generation of European
285   Reanalysis (ERA5) dataset land component (Muñoz-Sabater et al., 2021).   MERRA-2, produced
286   by NASA's Global Modelling and Assimilation Office (GMAO), used the Goddard Earth Observing
287   System (GEOS) model and analysis scheme and assimilated the latest observations. ERA5
288   reanalysis was developed by the European Centre for Medium-Range Weather Forecasts (ECMWF)
289   using the Carbon Hydrology-Tiled ECMWF Scheme for Surface Exchanges over Land
290   (CHTESSEL) driven by the downscaled meteorological forcing from the ERA5 climate reanalysis
291   (Hersbach et al., 2020). These reanalysis datasets are also used in extracting long- and shortwave
292   radiation, as well as u- and v-components of wind.
293   For AET, the REA dataset, which used the reliability ensemble averaging (REA) method to
294   merge ERA5, Global Land Data Assimilation System Version 2 (GLDAS2), and MERRA-2 is used
295   (Lu et al., 2021). Another AET data source is the product of the Global Land Evaporation
296   Amsterdam Model (GLEAM) based on satellite observations of surface net radiation and near-
297   surface air temperature (Martens et al., 2017). For PET, GLEAM is also incorporated. Another PET
298   dataset for GSHA is an hourly PET at 0.1° resolution for the global land surface (hPET) calculated
299   from ERA5-land wind speed, air and dew point temperature, net radiation components, and surface
300   air pressure (Singer et al., 2021).

301   3.4.2 Water storage term datasets

302   ERA5-land data is also applied in extracting soil moisture for 4 soil layers, as well as snow
303   water equivalence. For groundwater, an assimilation dataset from NASA's Gravity Recovery and
304   Climate Experiment (GRACE) and its follow-on mission (GRACE-FO) is used (Li et al., 2019).
305   The dataset merged water storage derived from GRACE satellite products into ECMWF Integrated
306   Forecasting System meteorological data-forced NASA's Catchment land surface model (CLSM).
307   The data is represented as groundwater drought indicator (GWI), which is the percentage of
308   groundwater storage estimates from the GRACE data assimilation relative to the climatology

309 (representing historical conditions), at weekly time scales from 2003-2021.

310 3.4.3 Land surface characteristic datasets

311 Global urban development for 1985-2015 is represented as the urban fraction in each watershed
312 using the global annual urban dynamics (GAUD) at 30-m resolution. The dataset was derived from
313 Landsat surface reflectance based on the Normalized Urban Areas Composite Index (NUACI) (Liu
314 et al., 2020). For forest and cropland fractions, the Terra and Aqua combined Moderate Resolution
315 Imaging Spectroradiometer (MODIS) Land Cover Type (MCD12Q1) land cover dataset, is used
316 (Friedl et al., 2010). It covers 2001-2020 with a resolution of 500 m, and the categories used for
317 GSHA are the International Geosphere–Biosphere Programme classification (IGBP) forests and
318 croplands. Another land cover is vegetation, which is represented by LAI obtained from the National
319 Oceanic and Atmospheric Administration (NOAA) Climate Data Record (CDR) of Advanced Very
320 High-Resolution Radiometer (AVHRR) product, which relied on artificial neural networks and
321 AVH09C1 surface reflectance product (Claverie et al., 2016).

322 3.4.4 Dams and reservoirs

323 The newly published Georeferenced global Dams And Reservoirs (GeoDAR) dataset that
324 documented the dam and reservoir construction years is used for building the temporally varying
325 watershed reservoir capacity and DOR. GeoDAR georeferenced the International Commission on
326 Large Dams (ICOLD) World Register of Dams (WRD), and geo-matched multi-source regional
327 registers and geocoding descriptive attributes through the Google Maps API (Wang et al., 2022).
328 The reservoir capacities are used together with the mean annual streamflow to obtain the DOR based
329 on equation $dor = SC/Q_{mean}$, where SC refers to reservoir storage capacity and Q_{mean} is the
330 mean annual streamflow in the corresponding year.

331 3.4.5 Static variables

332 We matched GSHA river IDs and HydroATLAS river reach IDs to link the static attributes.
333 HydroATLAS includes 56 variables for hydrology, physiography, climate, land cover & use, soils
334 & geology, and anthropogenic influences for over 8.5 million river reaches globally.
335
336 **Table 4 Data sources used for the GSHA variables.**

Category	Dataset	Resolution	Interval	Reference
Meteorology	MSWEP	0.25°	Daily	(Beck et al., 2017; Beck et al., 2019)
	EM-Earth	0.1°	Daily	(Tang et al., 2022)
	ERA5-land	0.1°	Hourly	(Muñoz-Sabater, 2019)
	MERRA-2	0.5°* 0.625°	Hourly	(GMAO, 2015)
	EUSTACE	0.25°	Daily	(Brugnara et al., 2019)
	REA	0.25°	Daily	(Lu et al., 2021)

	GLEAM	0.25°	Daily	(Martens et al., 2017; Miralles et al., 2011)
	hPET	0.1°	Daily	(Singer et al., 2021)
Water storage terms	ERA5-land	0.1°	Hourly	(Muñoz-Sabater, 2019)
	GRACE-FO data assimilation	0.25°	Weekly	(Li et al., 2019; Zaitchik et al., 2008)
Land surface	GAUD	30 m	Yearly	(Huang, 2020)
	MCD12Q1	500 m	Yearly	(Friedl et al., 2019)
	CDR Leaf Area Index	0.05°	Daily	(Vermote et al., 2019)
Dam and reservoir	GeoDAR	NaN (polygon)	Yearly	(Wang et al., 2022)
Static Attributes	HydroATLAS	NaN (line)	NaN (static)	(Lehner et al., 2022; Linke et al., 2019)

3.5 Variable extraction methods

For grid data with relatively coarse spatial resolutions (≥0.05°), we used an area-weighted approach to extract the variable (Addor et al., 2017) based on the proportion of the grid area contained in the basin boundary, while for high-resolution grid data, we extracted the arithmetic mean directly. **Figure 4** shows the area-weighted average approach we used for grid data with spatial resolution ≥0.05° to reduce the influence of watershed area on data uncertainty (Tang et al., 2022). The grid data (**4a**) and the quality-controlled watersheds (**4b**) were overlayed and all grids intersecting with the watershed were obtained (**4c**). For each intersected grid, the proportion of the polygon in the grid was calculated as the weight (dark blue, **4d**); the product of the weight and the corresponding grid value was calculated over all intersected grids (**4e**) and were summed up as the weighted average (**4f**). For wind, the u- and v-wind components were first used to calculate wind speed, then the basin average was calculated with the weighted average approach. For grid data with a spatial resolution of <0.05°, the area-weighted approach was not adopted as it offers limited gains while becoming computationally too expensive. For reservoirs, we used the reservoir polygons in GeoDAR, which were spatially joined to GSHA watershed polygons. All the intersected reservoirs were considered contributory to the management of the corresponding watershed and were used to calculate the total reservoir storage capacity and degree of regulation.
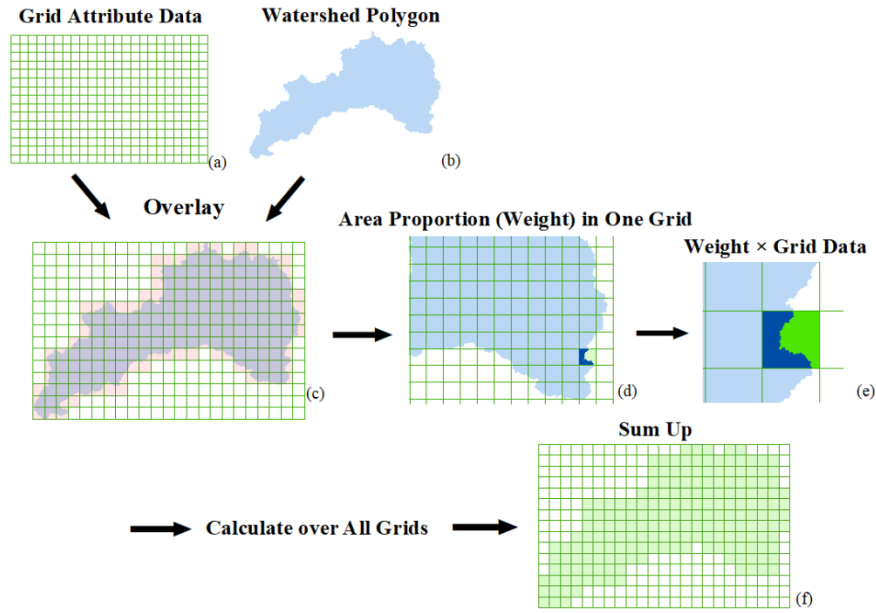
354
355 **Figure 4 Determination of the area weights in extracting gridded data to GSHA watershed**
356 **polygons.** This weighted approach is applied to data at a resolution of ≥0.05° but not for data at a finer
357 spatial resolution due to computational costs.

358 3.6 Uncertainty estimates

359   We also provided uncertainty estimates of the meteorological variables by calculating the long-
360 term mean of each dataset in each watershed, where the discrepancy between the maximum and
361 minimum among the data sources (X_{max} and X_{min}) as a percentage of their mean ($\bar{X}$) was used
362 in the uncertainty estimation (see Eq. 1):

$$uncertainty = \frac{X_{max}-X_{min}}{\bar{X}} * 100\%, \qquad (1)$$

363

364

365 3.7 Validation

366   After delineation, we validated our watershed areas with officially reported watershed areas
367 from BOM, HYDAT, and GRDC by matching GSHA watersheds by their agency IDs. We set the
368 criteria of mismatched watersheds as (1) the area difference being over $\pm20\%$ of the officially
369 reported area, and (2) the area ratio being less than 0.1 or over 10 times the reported areas. Since
370 not all agency websites reported watershed areas, thus we added a flag field in the attributes as
371 "unverified", "verified match", and "verified mismatch" to allow users to filter the watersheds
372 flexibly and avoid putting the samples in the dataset under an unfair standard.
373   Postprocessing of the extracted variables includes the unification of units and manual quality
374 checks. For streamflow characteristics, we validated three of our indices against GSIM for its global
375 coverage, including the mean annual streamflow, 10th and 90th percentiles. The spatial joint between
376 GSHA and GSIM gauges in a 10 km buffer zone was performed, and only the GSIM gauge with a

377   minimum distance and watershed area difference ≤5% to a GSHA gauge was considered. Pairs
378   with 0 measurements were excluded and 9835 pairs were involved eventually. We plotted the scatter
379   plot of GSHA-GSIM mean flow, 10th and 90th percentiles, and compared the fitting line to the 1:1
380   line, with correlation coefficients calculated (see Section 4.1).

381   We also validated precipitation, potential ET, and 2 m air temperature with the regional
382   CAMELS-US dataset. We compared the Daymet meteorological variables of CAMELS and the
383   mean of GSHA variables for validation. Since we included ERA5 data for most of our variables
384   directly or indirectly as the data source, while Caravan consistently used ERA5, we did not use
385   Caravan for the global validation as it is not considered as fully independent from GSHA. The
386   spatial match was the same as we did for GSIM which resulted in 906 pairs. This number was larger
387   than the total CAMELS gauge numbers as some gauges might be repeatedly paired due to location
388   bias of the USGS gauges and MERIT river networks, as well as the adjacency between gauges of
389   different agencies. Similarly, scatter plots and correlation coefficients are provided for assessment.

3.8 Watershed classification and change detection

391   We classified the watersheds as natural and human-managed to analyse the influence of human
392   water management. A watershed is classified as a natural watershed if it satisfies the following: (1)
393   DOR is smaller than 10%; (2) the urban extent is less than 5%; and (3) the sum of urban and cropland
394   fractions is smaller than 10% (L. Yang et al., 2021; Zhang et al., 2023). The classification was
395   performed for 2001-2015, and the changing patterns of the watersheds are divided into six categories:
396   (1) natural (N) when the watershed remained natural for all 15 years; (2) human managed (H) when
397   the watershed remained human managed for all 15 years; (3) natural to human managed (NH) when
398   the watershed was first natural in 2001, but changed to and maintained human managed later; and
399   (4) human managed to natural (HN) when the watershed was first human managed in 2001, but
400   changed to and maintained natural later.

4 Results

402   As previous studies have already revealed the spatial patterns of the LSH hydrometeorological
403   variables both locally and globally, here we put the spatial patterns of GSHA meteorological
404   variables and streamflow indices in **Appendix A**, while we focus on using the Results section to
405   reveal the uniqueness of GSHA. These include a technical validation of GSHA, uncertainty analysis,
406   and the temporal change of watershed human management levels.

4.1 Technical validation

408   The validation result figures of watershed areas are in **Appendix B** since we focused more on
409   the variables and already added the validity results in the dataset as "unverified", "verified match",
410   and "verified mismatch" fields in the dataset. Under our criterion of filtering "mismatch" watersheds,
411   1.9% of BOM watersheds, 4.7% of HYDAT watersheds and 8.9% of GRDC watersheds are

412 mismatched. After removing these watersheds, correlation coefficients between GSHA and the
413 agencies can reach 0.99, which verified the correctness of our watershed delineation and data
414 extraction approach.

415 **Figure 5** illustrates the validation results of GSHA. **Figures 5a–5c** show streamflow indices
416 as validated against GSIM globally, and **Figures 5d–5f** show meteorological variables as validated
417 against Daymet from CONUS CAMELS. For streamflow indices, precipitation, and temperature,
418 the correlation coefficients exceed 0.95 (significance p<0.01), and the fitting lines are close to the
419 1:1 line, indicating high consistencies between GSHA and the reference datasets. For PET, however,
420 the coefficient is low, at only 0.573 (significance p<0.05), and the CAMELS PET is generally higher
421 than GSHA ensemble, which is possibly ascribed to the high uncertainty among PET datasets that
422 is yet to be fully resolved (Singer et al., 2021) (see **Appendix C**). Note that the gauge pairing might
423 bring a small proportion of wrong pairs for some very close gauges, and differences in temporal
424 ranges of GSHA and GSIM might cause some discrepancies for observed streamflow.
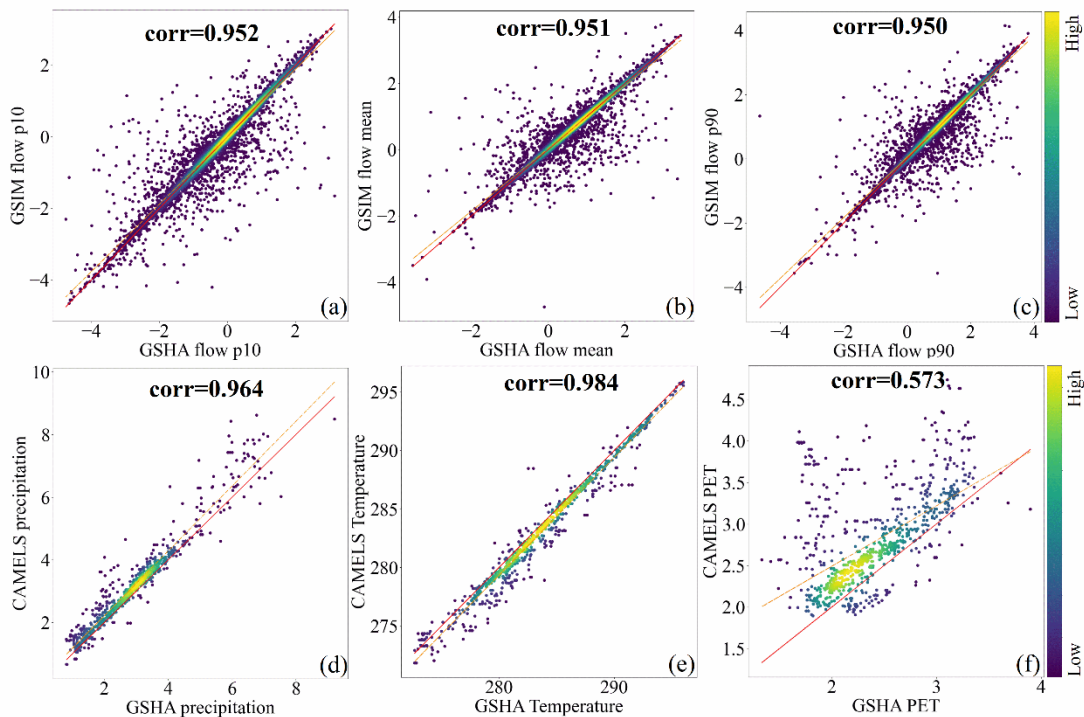
425
426 **Figure 5 Validation of GSHA with GSIM streamflow characteristics ((a), (b) and (c)), and**
427 **CAMELS meteorological variables ((d), (e) and (f)).** 'Corr' in the subfigure is the Pearson correlation
428 coefficient. The red line is the 1:1 line, while the orange dotted line is the fitting line of the scatter points.
429 The colour bar represents density of the sample points. The unit of X and Y axes in (a), (b). and (c) is
430 long10 m³/s.

431 4.2 Uncertainty patterns for the GSHA meteorological variables

432 **Figure 6** shows the distributions of the uncertainties for different variables, and the colour bars
433 are unified to allow for comparisons between different variables.

434
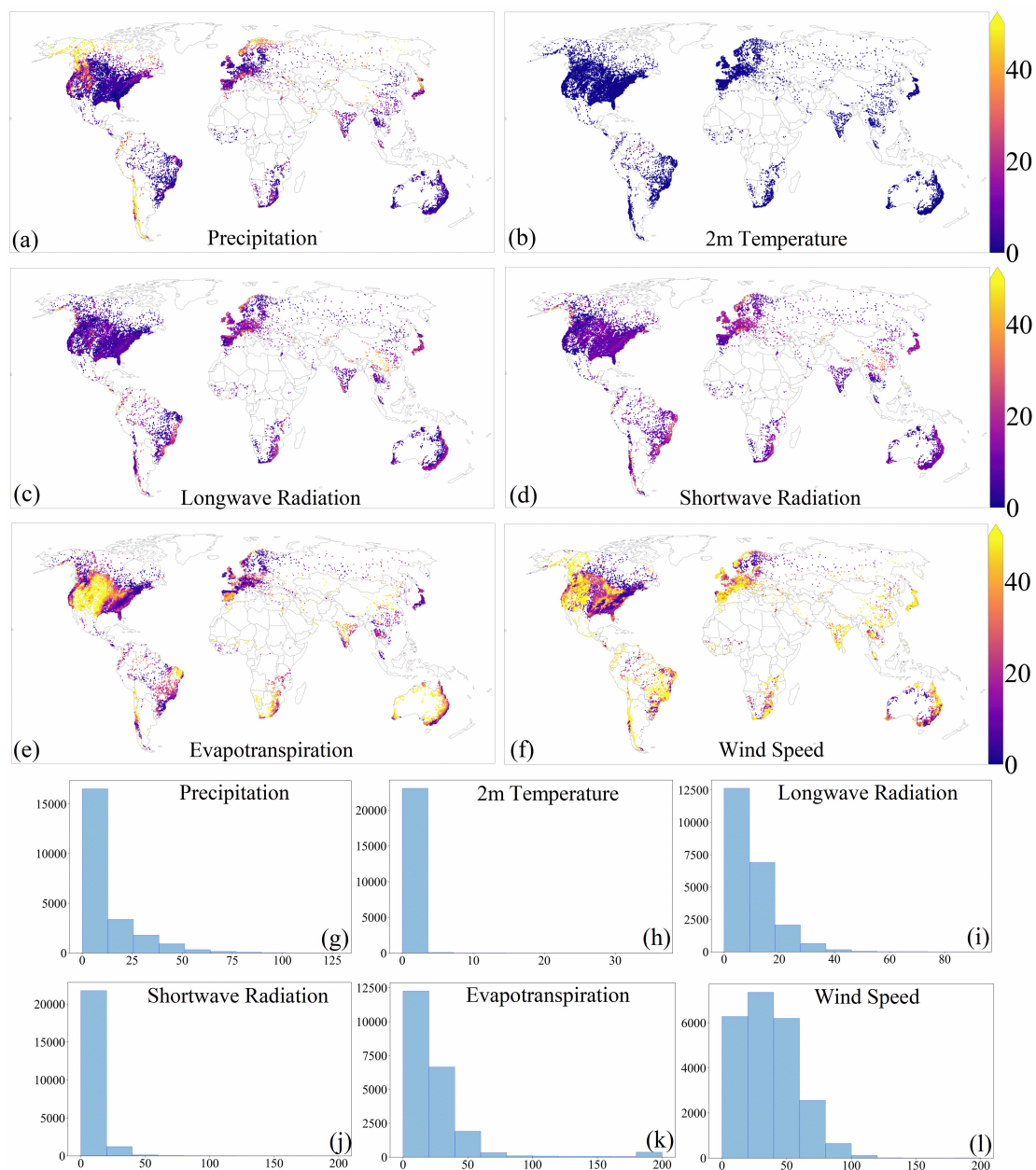
Figure 6 Global patterns of the uncertainty for the GSHA meteorological variables (in percentage). This includes the uncertainty (a) for precipitation (mm/day), (b) 2-m temperature (K), (c) longwave radiation (W/m²), (d) shortwave radiation (W/m²), (e) evapotranspiration (mm/day), and (f) wind speed (m/s), and (g) the uncertainty histogram for precipitation, (h) 2-m temperature, (i) longwave radiation, (j) shortwave radiation, (k) evapotranspiration, and (l) wind speed.

435
436
437
438
439
440

Generally, among all variables, air temperature (**Figures 6b & 6h**) shows the minimum uncertainty (<5%), suggesting high consistency of air temperature estimates from different datasets. The uncertainty for wind speed (**Figure 6f**) is the highest among all variables. Uncertainties for other variables show strong spatial variability. For example, uncertainties for precipitation are high in high-latitude or mountainous areas like the Rocky Mountains, northern Europe, the Alps, and the Andes areas (**Figure 6a**). This is reasonable because limited accessibility to in-situ observations and the misestimation of snow (Schreiner-McGraw & Ajami, 2020) can contribute to precipitation

441
442
443
444
445
446
447

448   estimation errors, while the data sources show relatively high consistency (*uncertainty* ≤25%) in

449   other parts of the world (**Figure 6g**). For radiation, as solar/shortwave radiation is largely affected

450   by sky conditions, uncertainties are high in regions with less clear sky, including south-west China

451   and its surrounding areas, high latitude regions of the northern hemisphere, and Europe (Brun et al.,

452   2022). These places are also subject to high thermal/longwave radiation uncertainties for similar

453   reasons (**Figure 6c**). Land cover including vegetation and artificial surface, is another factor

454   influencing surface net radiation through the albedo effect (Hu et al., 2017), thus for heavily

455   vegetated and urbanized areas, such as the Amazon region and east coastal Australia, uncertainties

456   for both longwave and shortwave fluxes are also relatively high. Nevertheless, **Figures 6i & 6j**

457   demonstrate that for the majority of watersheds, radiation uncertainties are < 25%, indicating that

458   the radiation data sources are generally consistent with each other. ET uncertainties are generally

459   larger than the above variables (**Figures 6e & 6k**), and are particularly prominent in dry areas of the

460   globe, e.g., central North America, northern Andes, central Asia, and Australia's grasslands and

461   deserts. It is also prominent in agriculture intensive regions like India and the northern part of China

462   (Sörensson & Ruscica, 2018), where agricultural irrigation may be the contributing factor to the ET

463   uncertainty. The spatial distributions of wind speed do not seem to show clear regional patterns

464   (**Figure 6f**), and uncertainty values of wind speed are generally larger over the majority of

465   watersheds (**Figure 6l**). Nevertheless, the uncertainties are low in Appalachia and northern Europe,

466   and are high in most parts of Brazil, the Andes, Africa, eastern and southern parts of Asia, as well

467   as Australia (**Figure 6f**). As we already selected relatively high-quality datasets for the variables,

468   these areas might be calling for more attention by the LSH developers, while providing possible

469   explanations for the inconsistencies in interpreting results or understanding the challenges in

470   estimating model parameters by the LSH users.

471
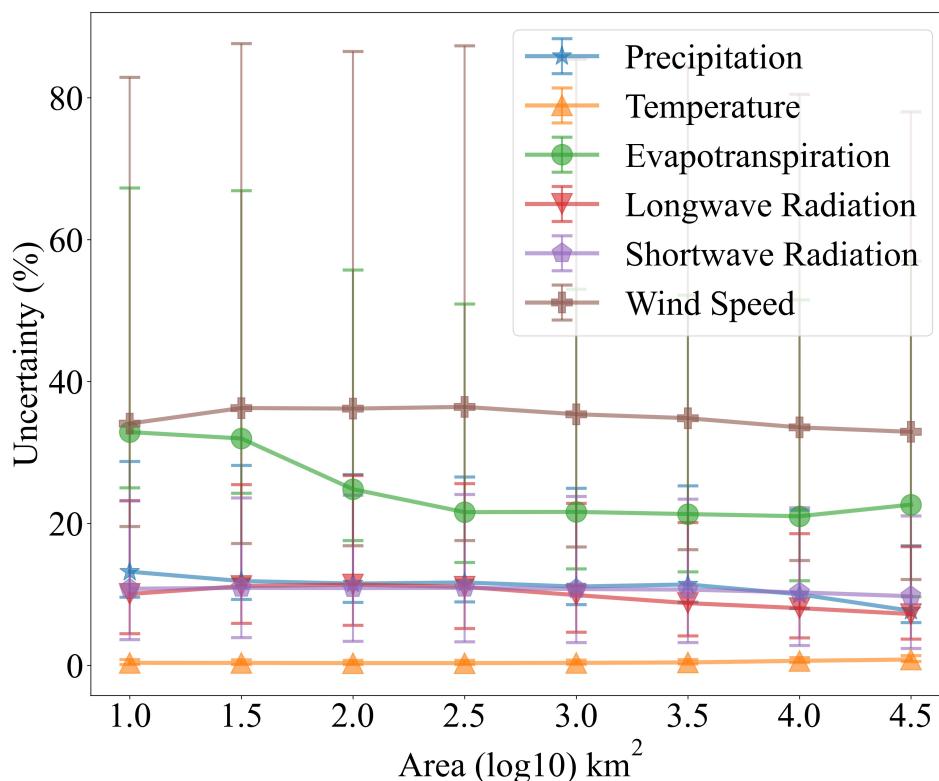
Figure 7 Relationship between variable uncertainties and watershed areas. The markers indicate mean values of the variable uncertainties in watersheds smaller than the corresponding x-axis value. The error bars represent the range between 25 and 75 percentiles of the uncertainty values.

Apart from the spatial patterns above, we also investigated the emergent patterns of the uncertainties. Existing studies indicate small basins can show larger uncertainties due to coarse resolution data inputs (Kauffeldt et al., 2013), while sub-grid variabilities might be offset by averaging over large watersheds. As we plotted the uncertainty against watershed areas in **Figure 7**, it verifies that for most variables, the uncertainty declines as the watershed area increases. **Figure 7** also reveals some interesting patterns which were rarely discussed in existing studies. For example, the most obvious decline of data uncertainty with area came from ET (green). ET is highly dependent on and significantly affected by land surface spatial heterogeneity, thus it benefits the most from spatial averaging for large river basins. Longwave radiation uncertainty (red) experiences a moderate decline, likely due to its linkage with land surface complexity and cloud conditions. Shortwave radiation and precipitation uncertainty show a similar decline pattern (blue and purple), which is possibly related to their strong ties to cloud covers. Temperature has a low uncertainty, and its relationship to watershed area is also not obvious. Wind speed uncertainty only declines slightly as the area increases, and this may be because wind speed uncertainty can be traced back more to the atmospheric circulation patterns instead of land surface conditions, thus showing a non-prominent relationship with watershed area. Overall, GSHA provides uncertainty estimates that capture these prominent patterns, which can be helpful to hydrologic modellers and users.

4.3 Natural and human managed watersheds and changing patterns

We also demonstrate the other key features of GSHA by categorizing global watersheds into natural and human-managed, and more prominently their temporal shifts in **Figure 8**. Overall, the majority of human-managed watersheds are located in the US, Europe, and other regions with intensive industrial or agricultural activities such as East and South Asia (**Figures 8a and 8b**). During 2001-2015, 46.89% of the watersheds remained natural, while another 47.62% under human management in 2001 remained in the category throughout the study period (**Figure 8d**). Generally, the northern hemisphere has a larger proportion of human-managed watersheds, while watersheds in the less populated and urbanized southern hemisphere largely remain natural.

Noticeably, 4.36% of GSHA watersheds switched from natural to human-managed (1011 watersheds), and the remaining 1.13% changed back to natural states from human managed during 2001-2015. For instance, watersheds in the middle and lower Yangtze River area and the north-eastern China show a shift from human-managed to natural state, where ecological restoration projects were in place (Qu et al., 2018; Zhang et al., 2015). Although the time span of GSHA LULC dynamics restricted the change detection for developed countries as their urbanizations and infrastructure developments have long been completed, and for fast emerging economies after 2015, the time series were also missing; nevertheless, the changing human activities captured by GSHA may be helpful to understand the streamflow changes including flood characteristics (Yang et al., 2021; Zhang et al., 2022).
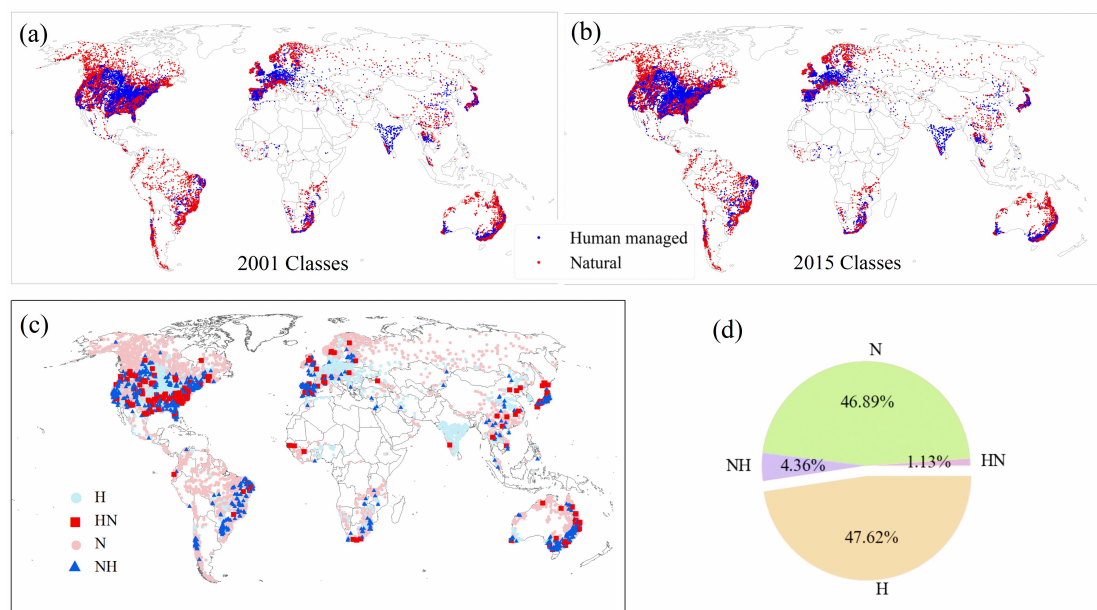
Figure 8 Classification of natural and human managed watersheds in 2001 (a) and 2015 (b). Changes in watershed categories are illustrated by (c) and (d). H and N in (c) and (d) represent watersheds that maintained human managed or natural from 2001-2015; NH and HN represent those changing from natural to human managed and from human managed to natural, respectively.

We further used several examples to illustrate the changing status of GSHA watersheds (**Figure 9**). **Figures 9a and 9b** show a watershed located in Northeast China, where the rapid increase in

cropland shifted the watershed from natural states to human-managed in recent years. **Figures 9c and 9d** correspond to a mountainous area in Sichuan Province, China, which became human-managed due to the construction of a reservoir in 2006. For another case in Northeast China (**Figures 9e and 9f**) and a USGS case (**Figures 9g and 9h**), the watersheds shifted from human-managed to natural, which is mainly manifested by the reduction in cropland fraction due to the environmental policy. For instance, afforestation in response to an appeal of sustainable agriculture policy (Du et al., 2023) during 2000-2010 in Changbai Mountains where the watershed in **Figures 9e and 9f** is located, significantly increased the forest cover and might bring a decline in human disturbance in the form of land use (Zhang & Liang, 2014). These results highlight the shifting watershed status that would require further attention from LSH users, which is encapsulated in GSHA v1.1 and will be continuously improved in the future.
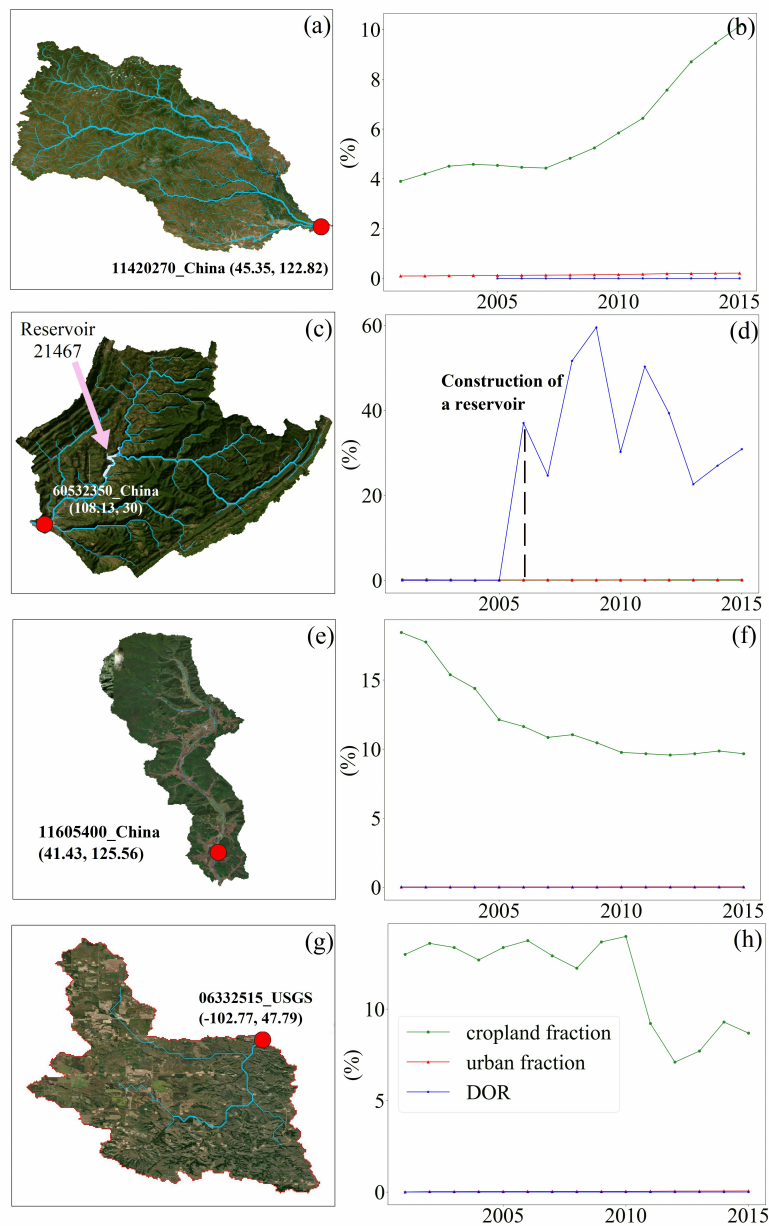
Figure 9 Cases for shifting status of the watershed classification. (a) and (b) correspond to 11420270_China, and (c) and (d) correspond to 60532350_China, both of which changed from natural

534   to human managed category. (e) and (f) represent11605400_China, and (g) and (h) correspond to
535   06332515_USGS watershed changing from human managed to natural watershed.

4.4 Changing runoff coefficient patterns derived from GSHA

537   Finally, we also analysed the global pattern in the trend of runoff coefficient (RC) as a brief
538 demonstration on what GSHA can offer out of its many potential usages. RC is defined as R/P,
539 where R denotes runoff (mm) and P denotes precipitation (mm). **Figure 10a** shows that regions with
540 high RC (i.e., a large proportion of rainfall goes into rivers instead of being evaporated or consumed)
541 are in east Asia and North America, most parts of Europe, the west coast of North America and the
542 Amazon, in general agreement with the aridity patterns across the globe. For arid/semiarid areas
543 and places with intense water use (e.g., western US, eastern Brazil, Australia, Africa), RC is low,
544 meaning most of the precipitation does not reach the gauged river.
545   We found that RC generally remained stable for the past decades (i.e., grey dots in **Figure
546 10b**; >80% of the gauges did not observe a statistically significant trend), while 4252 watersheds
547 observed a statistically significant trend in RC at 95% level (5690 watersheds at 90% level). Among
548 them, decreasing RC is more widespread than increasing RC. The most pronounced decreasing
549 trends are observed in Europe, India, eastern Brazil, Chile, eastern Australia, and the Euphrates and
550 Tigris, which largely correspond to regions with known intense agricultural, industrial, and
551 residential water use that may have reduced the river water. We note that the global RC trend patterns
552 were different from a recent study that showed mostly increasing RC in the high-latitudes, central
553 North America, eastern Australia, and Europe (Xiong et al., 2022). Given Xiong et al. (2022) used
554 estimated runoff while we used runoff directly from gauge observations, it is likely that the
555 concerning water availability issues in the context of increasing human water use may not be fully
556 captured by existing studies. Regional studies also tend to show inconsistent results. For example,
557 a study based on models incorporating climate change and land use change but ignoring human
558 water consumptions suggested that deforestation and urbanization generally increase RC (Lucas-
559 Borja et al., 2020), while another study identified a significant decreasing trend for RC by focusing
560 on cases with intense irrigational water use (Banasik and Hejduk, 2012). These collectively preclude
561 a clear identification of consistent RC trends (Velpuri and Senay, 2013) and a clear causal factor
562 attribution analysis given the complexity of the anthropogenic factors. As such, GSHA may offers
563 a new path to fill in the gap of disentangling the influences of large-scale water use on decreasing
564 RC.

565
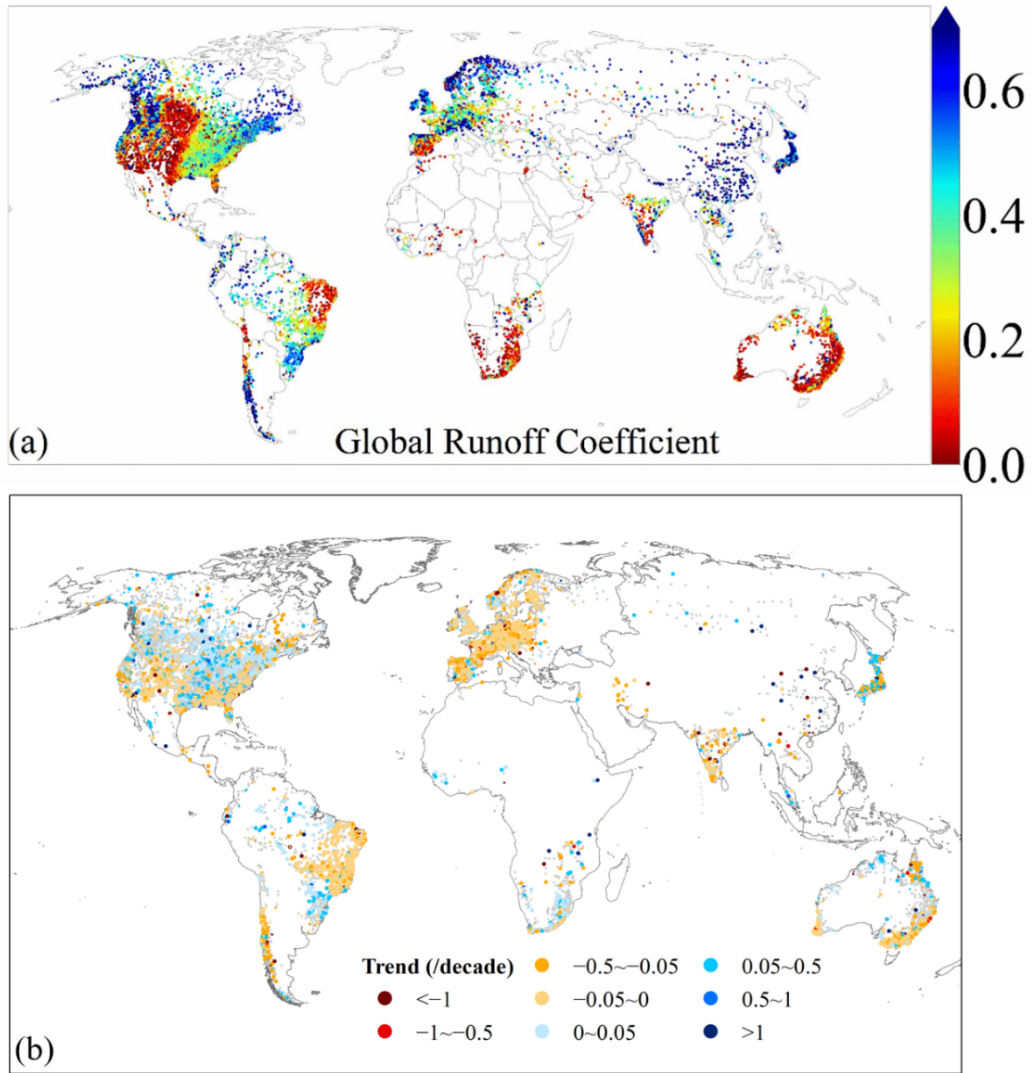
Figure 10 Patterns of runoff coefficient (a) and its trend (b). Only watersheds with statistically
significant trend (p<0.05) are shown with colours in (b); the small and large sized points represent 95%
(p<0.05) and 90% significance level (p<0.1), respectively. Note that the temporal coverage is different
for different gauges; readers can refer to the GSHA temporal coverage for interpreting the patterns. The
figure illustrates 18987 GSHA watersheds. Watersheds with less than 10 years of indices calculated
from over 250 valid observations per year, as well as with runoff coefficient trend over 20 per decade,
are not demonstrated in subfigure b.

5 Conclusions

Large sample hydrology (LSH) datasets play a critical role in data-driven analyses and model
parameter estimation for hydrological studies. From MOPEX (Duan et al., 2006) to Caravan
(Kratzert et al., 2023), significant efforts have been made to improve the comprehensiveness of LSH,
yet issues related to data spatial coverage, uncertainty estimates, and human activity dynamics
remain to be solved. This study complements existing LSH with a new synthesis dataset named the

579   Global Streamflow characteristics, Hydrometeorology, and catchment Attributes for large sample

580   river-centric studies (GSHA v1.1).

581   To summarize, GSHA contributes the following aspects to the LSH development:

582   1.   It includes streamflow indices, hydrometeorological data, and surface characteristics data for

583   21568 gauges compiled from 13 agencies worldwide, which represents one of the most

584   comprehensive LSH by far.

585   2.   We incorporated multiple data sources to provide uncertainty estimates for each meteorological

586   variable (including precipitation, 2 m air temperature, radiation, wind, and ET). The spatial

587   patterns and the relationship between the uncertainty and the watershed characteristics GSHA

588   reveals may be helpful to identify inconsistencies among data-driven studies or biases for model

589   parameter estimation studies using existing LSH.

590   3.   Dynamic data are provided for previously static data descriptors for land cover changes

591   including urban, cropland and forest fractions, as well as reservoir storage change including

592   storage capacity and degree of regulation.

593   Although GSHA does not cover watersheds of $<25km^2$ or the dynamics of cryosphere variables

594 (e.g., glacier and permafrost) that have become increasingly important in terrestrial hydrological

595 changes, and the time spans for the dynamic descriptors of LULC are unable to cover the critical

596 periods for the advanced and less-advanced economies due to the constraints with existing LULC

597 data, GSHA is expected to be utilized to unravel the following insights:

598   1.   The uncertainty patterns vary between variables and geographical regions, indicating that the

599   interpretation of model and analysis results need to consider inconsistencies of raw data, apart

600   from looking into the methodologies and patterns themselves.

601   2.   Although most watersheds have remained natural or human managed throughout the GSHA

602   time span, a considerable number of watersheds shifted between the two categories, which can

603   be ascribed to urbanization, cropland increase, reservoir construction and ecological restoration

604   such as returning farmland to natural states, and these can be clearly manifested using GSHA.

605   3.   Analysis with runoff coefficient reveals that among gauges with a statistically significant trend,

606   a greater portion experienced a declining RC trend than an increase trend. This pattern revealed

607   by GSHA can be used to further study water availability issues in a changing climate.

608   As our knowledge on the above processes continues to improve, we expect that future versions

609 of GSHA will be continuously updated. Finally, better hydrological data sharing is crucial to

610 advance global change hydrology studies.

611 # Appendix

612 ## A. Spatial patterns of GSHA meteorological variables

613   **Figures A1 & A2** show the spatial distributions of GSHA meteorological variables and selected

614 streamflow indices. The spatial pattern derived from each individual data source is plotted separately.

615
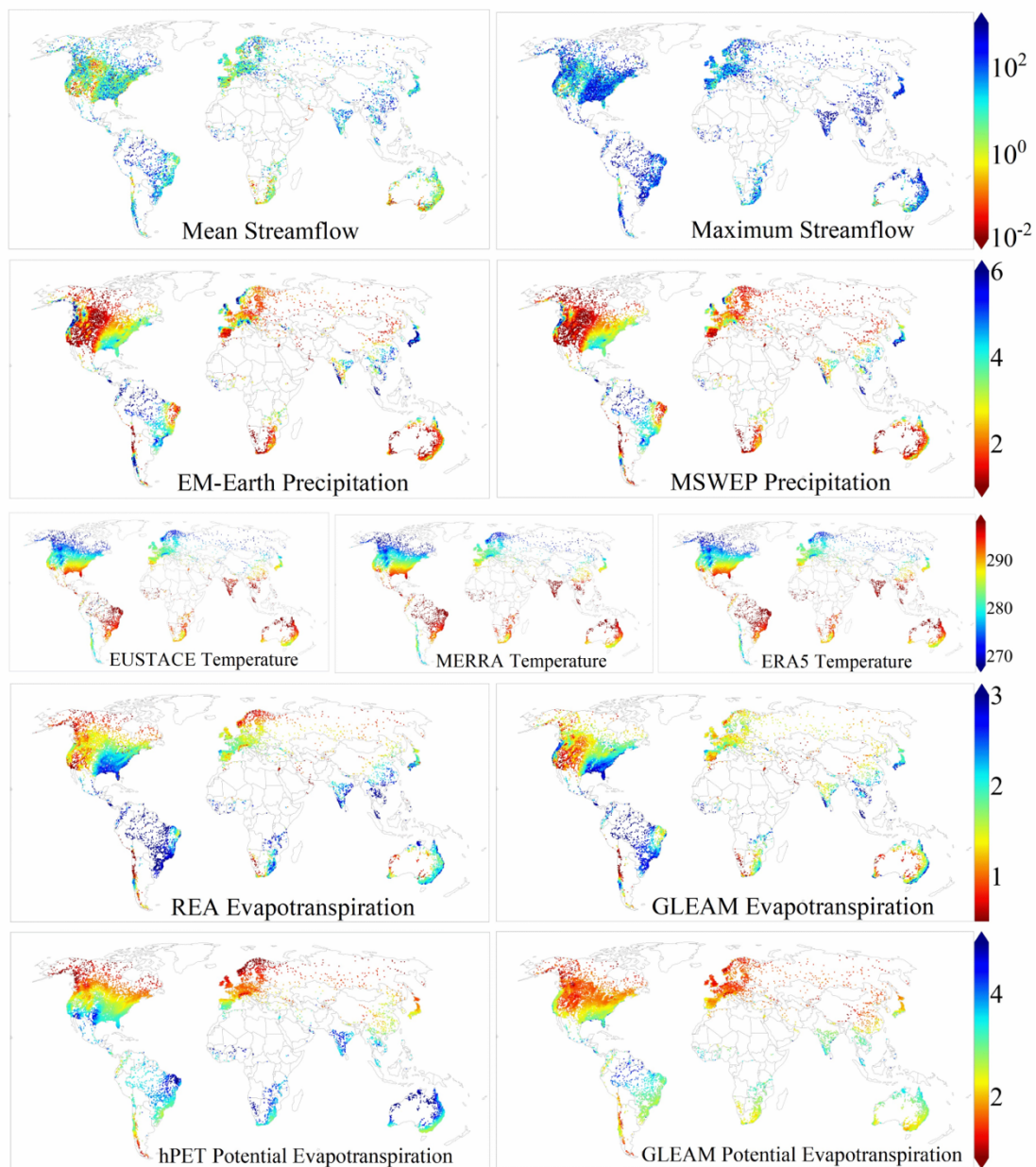
Figure A1 Spatial distribution of streamflow indices (row 1, m³/s), precipitation (row 2, mm/day), 2 m air temperature (row 3, K), actual ET (row 4, mm/day), potential ET (row 5, mm/day).
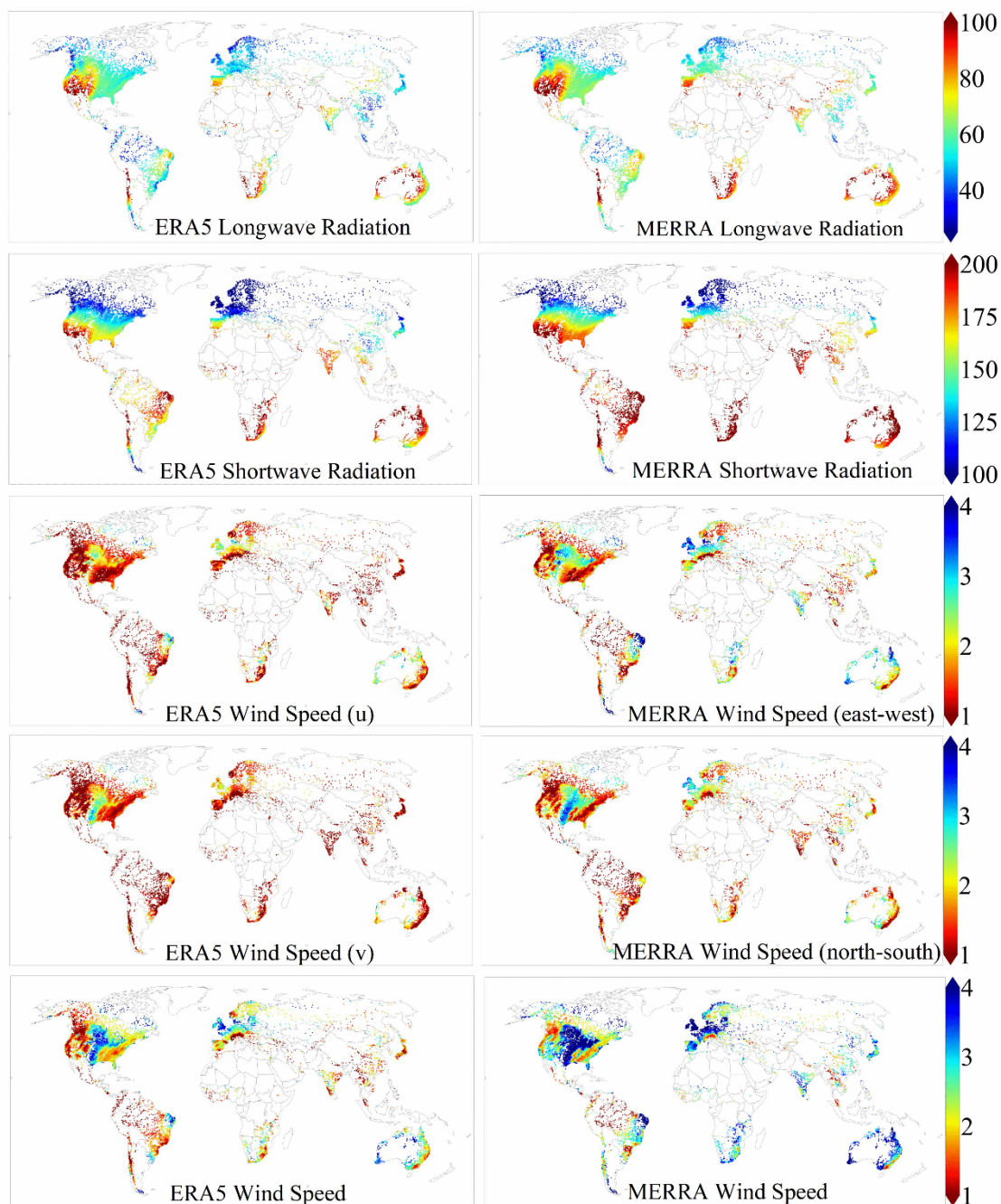
Figure A 2 Spatial distribution of longwave radiation (row 1, W/m^2), shortwave radiation (row 2, W/m^2), wind u- (row 3, m/s) and v- components (row 4, m/s) and the wind speed (row 5, m/s).

B. Validation results of watershed areas

The validation results with BOM, HYDAT, GRDC, and USGS on watershed areas are plotted in **Figure B1,** where the mismatches between GSHA areas and the officially reported areas are shown. Before removing the mismatched watersheds, their correlation coefficients are 0.960, 0.840, 0.709, 0.905, respectively, as showm in **Figure B1 (a), (b), (c), and (d).** After removing the mismatched watersheds, correlation coefficients for all three agencies reach 0.999, as shown in

Figure B1   (e), (f), (g) and (h). As we traced the MERIT Basins (Lin et al., 2019) for our watershed delineation, the mismatches are believed to occur when the gauge locates in the vicinity of the intersection point of a river reach and its main stream, which makes it difficult to decide which reach the gauge belongs to while matching the gauge to the MERIT river network. This explains why in **Figure B1** most of the mismatches appear at relatively small areas. As we do not have access to all official watershed areas, and **Figure B1 (a), (b), (c) and (d)** suggest that matching qualities differ among the agencies, to simply remove the mismatched watersheds or to modify them might put the samples in the dataset under an unfair standard. Additionally, some agencies such as GRDC experienced some updates of their gauige locations and upstream areas, thus watershed boundaries in all datasets mentioned might come with uncertainties. Therefore, we gave the watersheds as "unverified", "verified match", and "verified mismatch" identifiers to allow users to flexibly filter the watersheds.
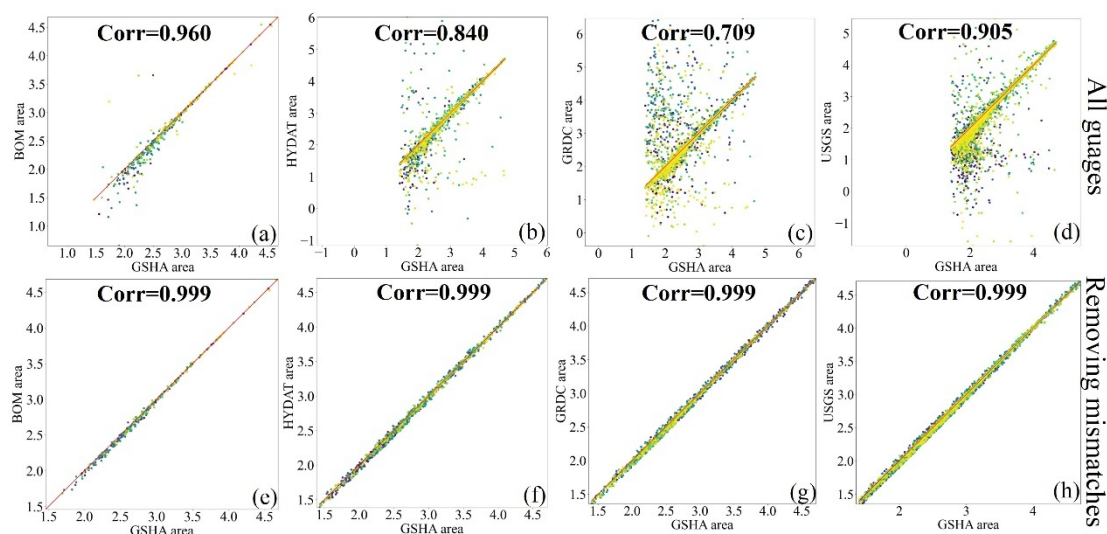
Figure B1 Validation of GSHA with officially reported areas of BOM (a, e), HYDAT (b, f), GRDC (c, g), and USGS (d, h). Subfigures (a) to (d) are the results before removing the mismatched watersheds, and subfigures (e) to (h) represent results after removing the mismatched watersheds. The Pearson correlation coefficient are represented by "Corr" in the figure. The areas are represented by the unit of (log10 km^2).

C. Potential evapotranspiration uncertainty

The spatial and numerical distributions of potential evapotranspiration (PET) uncertainties are illustrated in **Figure C1** and **Figure C2**. PET uncertainty is high compared with other variables (see 5.2 section). The majority of high PET uncertainty watersheds are in dry areas, but since it is calculated from meteorological variables, exceptions exist for palces including eastern Pacific coast, where the climate is dry but PET uncertainty is low, and India, which is located in a wet climate zone but has high PET uncertainty. As demonstrated by **Figure C3**, PET uncertainty do not decrease with the increase of watershed area, probably because PET is calculated from various variables, and the calculation over large watersheds involves more uncertainties for individual grids.
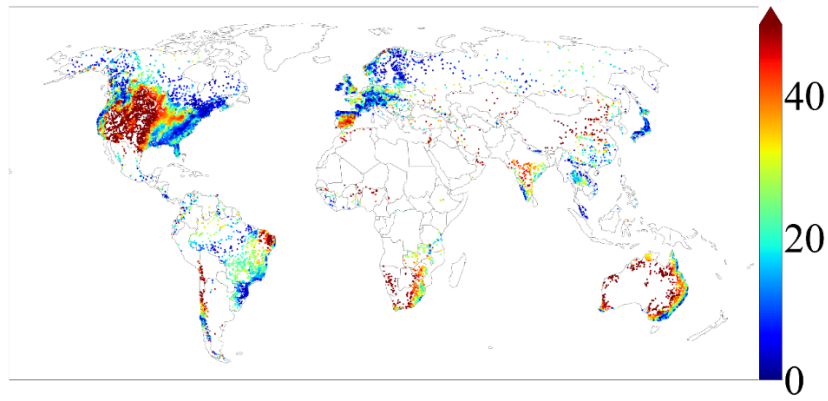
655
656   **Figure C1** Spatial pattern of potential evapotranspiration (PET) uncertainty.
657
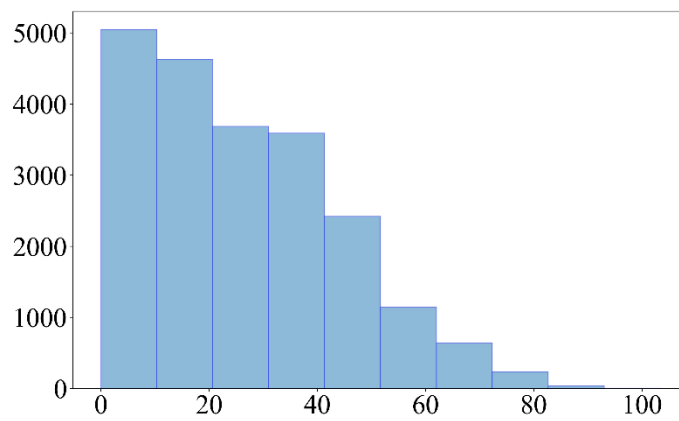
658
659   **Figure C2** Numerical distribution of PET uncertainty.
660
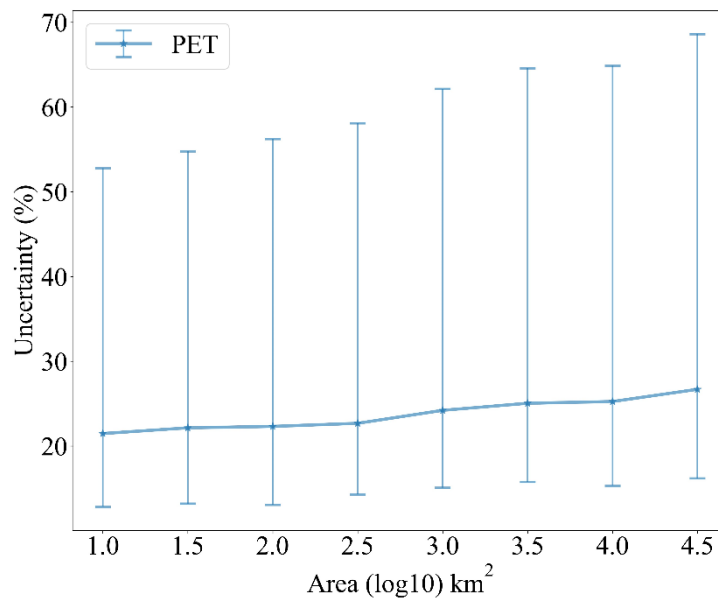
661
662   **Figure C3** Relationship of PET uncertainty to watershed area.

Author contribution

Conceptualization: PL. Investigation: ZY, PL, RR, GA, XL. Data curation: ZY, RR, XL, PL, ZZ, SC. Funding acquisition: PL. Writing - initial: ZY, PL. Writing - Review and Editing: PL, ZY, GA, RR, XL.

Data and Code Availability

GSHA v1.1 is openly available at https://doi.org/10.5281/zenodo.8090704 and https://doi.org/10.5281/zenodo.10433905. The codes involved in the workflow will be available upon reasonable requests to the authors. The publicly available gauge databases involved in this dataset include ArcticNet (www.r-arcticnet.sr.unh.edu/v4.0/AllData/index.html), Australian Bureau of Meteorology (www.bom.gov.au/waterdata/), Brazil National Water Agency (www.snirh.gov.br/hidroweb/serieshistoricas), Canada National Water Data Archive (www.canada.ca/en/environment-climate-change/services/water-overview/quantity/monitoring/survey/data-products-services/national-archive-hydat.html), Chile Center for Climate and Resilience Research (https://explorador.cr2.cl/), The Global Runoff Data Centre (https://portal.grdc.bafg.de/applications/public.html?publicuser=PublicUser), India Water Resources Information System (https://indiawris.gov.in/wris/#/RiverMonitoring), Japanese Water Information System (www1.river.go.jp/), Spain Annuario de Aforos (http://datos.gob.es/es/catalogo/e00125801-anuario-de-aforos/resource/4836b826-e7fd-4a41-950c-89b4eaea0279), Thailand Royal Irrigation Department (http://hydro.iis.u-tokyo.acjp/GAME-T/GAIN-T/routine/rid-river/disc_d.html), and the U.S. Geological Survey (https://waterdata.usgs.gov/nwis/rt). The Chinese Hydrology Project data was provided by the authors of the dataset (Henck et al 2010, Schmidt et al 2011).

Competing interests

The authors declare no conflict of interest.

Acknowledgements

This study is supported by the National Key Research and Development Program (2022YFF0801303), the Yunnan Science and Technology Major Project (202302AO370012), the Natural Science Foundation of China (42371481, 42175178), and the Fundamental Research Funds for the Central Universities to Peking University (7100604136).

References

Addor, N., Do, H. X., Alvarez-Garreton, C., Coxon, G., Fowler, K., & Mendoza, P. A. Large-sample hydrology: recent progress, guidelines for new datasets and grand challenges. *Hydrological Sciences Journal-Journal Des Sciences Hydrologiques*, *65*(5), 712-725. https://doi.org/10.1080/02626667.2019.1683182, 2020.

Addor, N., Nearing, G., Prieto, C.,Newman, A. J., Le Vine, N., & Clark, M. P. A ranking of hydrologicalsignatures based on their predictability in space. *Water Resources Research*, 54,8792–8812. https://doi.org/10.1029/2018WR022606, 2018.

Addor, N., Newman, A. J., Mizukami, N., & Clark, M. P. The CAMELS data set: catchment attributes and meteorology for large-sample studies. *Hydrology and Earth System Sciences*, *21*(10), 5293-5313. https://doi.org/10.5194/hess-21-5293-2017, 2017.

Aerts, J. P., Hut, R. W., van de Giesen, N. C., Drost, N., van Verseveld, W. J., Weerts, A. H., & Hazenberg, P. Large-sample assessment of varying spatial resolution on the streamflow estimates of the wflow_sbm hydrological model. *Hydrology and Earth System Sciences*, *26*(16), 4407-4430 , https://doi.org/10.5194/hess-26-4407-2022, 2022.

AghaKouchak, A., Chiang, F., Huning, L. S., Love, C. A., Mallakpour, I., Mazdiyasni, O., Moftakhari, H., Papalexiou, S. M., Ragno, E., & Sadegh, M. Climate Extremes and Compound Hazards in a Warming World. *Annual Review of Earth and Planetary Sciences, Vol 48, 2020*, *48*, 519-548. https://doi.org/10.1146/annurev-earth-071719-055228, 2020.

Alvarez-Garreton, C., Mendoza, P. A., Boisier, J. P., Addor, N., Galleguillos, M., Zambrano-Bigiarini, M., Lara, A., Puelma, C., Cortes, G., Garreaud, R., McPhee, J., & Ayala, A. The CAMELS-CL dataset: catchment attributes and meteorology for large sample studies - Chile dataset. *Hydrology and Earth System Sciences*, *22*(11), 5817-5846. https://doi.org/10.5194/hess-22-5817-2018, 2018.

Arsenault, R., Brissette, F., Martel, J.-L., Troin, M., Lévesque, G., Davidson-Chaput, J., Gonzalez, M. C., Ameli, A., & Poulin, A. A comprehensive, multisource database for hydrometeorological modeling of 14,425 North American watersheds. *Scientific Data*, *7*(1), 243. https://doi.org/10.1038/s41597-020-00583-2, 2020.

Banasik, K., and Hejduk, L. "Long-term changes in runoff from a small agricultural catchment." Soil and Water Research 7, no. 2 , 64-72. https://doi.org/10.1007/s10661-006-0769-2, 2012.

Beck, H. E., van Dijk, A. I., De Roo, A., Miralles, D. G., McVicar, T. R., Schellekens, J., & Bruijnzeel, L. A. Global-scale regionalization of hydrologic model parameters. *Water Resources Research*, *52*(5), 3599-3622. https://doi.org/10.1002/2015WR018247, 2016.

Beck, H. E., Van Dijk, A. I., Levizzani, V., Schellekens, J., Miralles, D. G., Martens, B., & De Roo, A. MSWEP: 3-hourly 0.25 global gridded precipitation (1979–2015) by merging gauge, satellite, and reanalysis data. *Hydrology and Earth System Sciences*, *21*(1), 589-615. https://doi.org/10.5194/hess-21-589-2017, 2017.

Beck, H. E., Wood, E. F., Pan, M., Fisher, C. K., Miralles, D. G., Van Dijk, A. I., McVicar, T. R., & Adler, R. F. MSWEP V2 global 3-hourly 0.1 precipitation: methodology and quantitative assessment. *Bulletin of the American Meteorological Society*, *100*(3), 473-500. https://doi.org/10.1175/BAMS-D-17-0138.1, 2019.

Belvederesi, C., Zaghloul, M. S., Achari, G., Gupta, A., & Hassan, Q. K. Modelling river flow in cold

and ungauged regions: A review of the purposes, methods, and challenges. *Environmental Reviews*, *30*(1), 159-173. https://doi.org/10.1139/er-2021-0043, 2022.

Benke, K. K., Lowell, K. E., & Hamilton, A. J. Parameter uncertainty, sensitivity analysis and prediction error in a water-balance hydrological model. *Mathematical and Computer Modelling*, *47*(11-12), 1134-1149. https://doi.org/10.1016/j.mcm.2007.05.017, 2008.

Beven, K. J., & Alcock, R. E. Modelling everything everywhere: a new approach to decision-making for water management under uncertainty. *Freshwater Biology*, *57*, 124-132. https://doi.org/10.1111/j.1365-2427.2011.02592.x, 2012.

Bourdin, D. R., Fleming, S. W., & Stull, R. B. Streamflow modelling: a primer on applications, approaches and challenges. *Atmosphere-Ocean*, *50*(4), 507-536. https://doi.org/10.1080/07055900.2012.734276, 2012.

Brugnara, Y., Good, E., Squintu, A. A., van der Schrier, G., & Brönnimann, S. The EUSTACE global land station daily air temperature dataset. *Geoscience Data Journal*, *6*(2), 189-204. https://doi.org/10.1002/gdj3.81, 2019.

Brun, P., Zimmermann, N. E., Hari, C., Pellissier, L., & Karger, D. N. Global climate-related predictors at kilometer resolution for the past and future. *Earth System Science Data*, *14*(12), 5573-5603. https://doi.org/10.5194/essd-14-5573-2022, 2022.

Brunner, M. I., Slater, L., Tallaksen, L. M., & Clark, M. Challenges in modeling and predicting floods and droughts: A review. *Wiley Interdisciplinary Reviews: Water*, *8*(3), e1520. https://doi.org/10.1002/wat2.1520, 2021.

Burges, S. J. Streamflow prediction: capabilities, opportunities, and challenges. *Hydrologic Sciences: Taking Stock and Looking Ahead*, *5*, 101-134, 1998.

Chagas, V. B., Chaffe, P. L., Addor, N., Fan, F. M., Fleischmann, A. S., Paiva, R. C., & Siqueira, V. A. CAMELS-BR: hydrometeorological time series and landscape attributes for 897 catchments in Brazil. *Earth System Science Data*, *12*(3), 2075-2096. https://doi.org/10.5194/essd-12-2075-2020, 2020.

Chen, X., Jiang, L., Luo, Y., and Liu, J.: A global streamflow indices time series dataset for large-sample hydrological analyses on streamflow regime (until 2022), *Earth Syst. Sci. Data*, 15, 4463–4479, https://doi.org/10.5194/essd-15-4463-2023, 2023.

Cho, K., & Kim, Y. Improving streamflow prediction in the WRF-Hydro model with LSTM networks. *Journal of Hydrology*, *605*, 127297. https://doi.org/10.1016/j.jhydrol.2021.127297, 2022.

Clark, M. P., Vogel, R. M., Lamontagne, J. R., Mizukami, N., Knoben, W. J., Tang, G., Gharari, S., Freer, J. E., Whitfield, P. H., & Shook, K. R. The abuse of popular performance metrics in hydrologic modeling. *Water Resources Research*, *57*(9), e2020WR029001. https://doi.org/10.1029/2020WR029001, 2021.

Claverie, M., Matthews, J. L., Vermote, E. F., & Justice, C. O. A 30+ year AVHRR LAI and FAPAR climate data record: Algorithm description and validation. *Remote Sensing*, *8*(3), 263. https://doi.org/10.3390/rs8030263, 2016.

Coxon, G., Addor, N., Bloomfield, J. P., Freer, J., Fry, M., Hannaford, J., Howden, N. J., Lane, R., Lewis, M., & Robinson, E. L. CAMELS-GB: hydrometeorological time series and landscape attributes for 671 catchments in Great Britain. *Earth System Science Data*, *12*(4), 2459-2483. https://doi.org/10.5194/essd-12-2459-2020, 2020.

Olivier Delaigue, Pierre Brigode, Vazken Andréassian, Charles Perrin, Pierre Etchevers, et al.. CAMELS-FR: A large sample hydroclimatic dataset for France to explore hydrological

778 diversity and support model benchmarking. *IAHS-2022 Scientific Assembly*, May 2022,
779   Montpellier, France. hal-03687235. https://doi.org/10.5194/egusphere-egu21-13349, 2022.

780 Do, H. X., Gudmundsson, L., Leonard, M., & Westra, S. The Global Streamflow Indices and Metadata
781   Archive (GSIM) - Part 1: The production of a daily streamflow archive and metadata. *Earth*
782   *System Science Data*, *10*(2). https://doi.org/10.5194/essd-10-765-2018, 2018.

783 Du, Z., Yu, L., Chen, X., Li, X., Peng, D., Zheng, S., Hao, P., Yang, J., Guo, H., Gong, P. An Operational
784   Assessment Framework for Near Real-time Cropland Dynamics: Toward Sustainable Cropland
785   Use in Mid-Spine Belt of Beautiful China. *Journal of Remote Sensing*. 2023;3:Article 0065.
786   https://doi.org/10.34133/remotesensing.0065, 2023

787 Duan, Q., Schaake, J., Andréassian, V., Franks, S., Goteti, G., Gupta, H., Gusev, Y., Habets, F., Hall, A.,
788   & Hay, L. Model Parameter Estimation Experiment (MOPEX): An overview of science strategy
789   and major results from the second and third workshops. *Journal of Hydrology*, *320*(1-2), 3-17.
790   https://doi.org/10.1016/j.jhydrol.2005.07.031, 2006.

791 Fang, Y., Huang, Y., Qu, B., Zhang, X., Zhang, T., & Xia, D. Estimating the Routing Parameter of the
792   Xin'anjiang Hydrological Model Based on Remote Sensing Data and Machine Learning.
793   *Remote Sensing*, *14*(18), 4609. https://doi.org/10.3390/rs14184609, 2022.

794 Fowler, K. J. A., Acharya, S. C., Addor, N., Chou, C. C., & Peel, M. C. CAMELS-AUS:
795   hydrometeorological time series and landscape attributes for 222 catchments in Australia. *Earth*
796   *System Science Data*, *13*(8), 3847-3867. https://doi.org/10.5194/essd-13-3847-2021, 2021.

797 Friedl, M. A., Sulla-Menashe, D., Tan, B., Schneider, A., Ramankutty, N., Sibley, A., & Huang, X.
798   MODIS Collection 5 global land cover: Algorithm refinements and characterization of new
799   datasets. *Remote Sensing of Environment*, *114*(1), 168-182.
800   https://doi.org/10.1016/J.RSE.2009.08.016, 2010.

801 Friedl, M., D. Sulla-Menashe. MCD12Q1 MODIS/Terra+Aqua Land Cover Type Yearly L3 Global 500m
802   SIN Grid V006., distributed by NASA EOSDIS Land Processes DAAC,
803   https://doi.org/10.5067/MODIS/MCD12Q1.006, 2019.

804 Gelaro, R., McCarty, W., Suárez, M. J., Todling, R., Molod, A., Takacs, L., Randles, C. A., Darmenov,
805   A., Bosilovich, M. G., & Reichle, R. The modern-era retrospective analysis for research and
806   applications, version 2 (MERRA-2). *Journal of Climate*, *30*(14), 5419-5454.
807   https://doi.org/10.1175/JCLI-D-16-0758.1, 2017.

808 Global Modeling and Assimilation Office (GMAO) , inst3_3d_asm_Cp: MERRA-2 3D IAU State,
809   Meteorology Instantaneous 3-hourly (p-coord, 0.625x0.5L42), version 5.12.4, Greenbelt, MD,
810   USA: Goddard Space Flight Center Distributed Active Archive Center (GSFC DAAC),
811   https://doi.org/10.5067/VJAFPLI1CSIV, 2015.

812 Gudmundsson, L., Do, H. X., Leonard, M., & Westra, S. The Global Streamflow Indices and Metadata
813   Archive (GSIM) - Part 2: Quality control, time-series indices and homogeneity assessment.
814   *Earth System Science Data*, *10*(2). https://doi.org/10.5194/essd-10-787-2018, 2018.

815 Gupta, H. V., Perrin, C., Bloschl, G., Montanari, A., Kumar, R., Clark, M., & Andreassian, V. Large-
816   sample hydrology: a need to balance depth with breadth. *Hydrology and Earth System Sciences*,
817   *18*(2), 463-477. https://doi.org/10.5194/hess-18-463-2014, 2014.

818 Hao, Z., Jin, J., Xia, R., Tian, S., Yang, W., Liu, Q., Zhu, M., Ma, T., Jing, C., & Zhang, Y. CCAM: China
819   catchment attributes and meteorology dataset. *Earth System Science Data*, *13*(12), 5591-5616.
820   https://doi.org/10.5194/essd-13-5591-2021, 2021.

821 Henck, A. C., Montgomery, D. R., Huntington, K. W., & Liang, C. Monsoon control of effective

discharge, Yunnan and Tibet. *Geology, 38*(11), 975-978. https://doi.org/10.1130/G31444.1, 2010.

Hersbach, H., Bell, B., Berrisford, P., Hirahara, S., Horányi, Á., Muñoz-Sabater, J., Nicolas, J. P., Peubey, C., Radu, R., Schepers, D., Simmons, A. J., Soci, C., Abdalla, S., Abellan, X., Balsamo, G., Bechtold, P., Biavati, G., Bidlot, J., Bonavita, M., . . . Thépaut, J. The ERA5 global reanalysis. *Quarterly Journal of the Royal Meteorological Society*, 146(730), 1999–2049. https://doi.org/10.1002/qj.3803, 2020.

Hrachowitz, M., Savenije, H., Blöschl, G., McDonnell, J., Sivapalan, M., Pomeroy, J., Arheimer, B., Blume, T., Clark, M., & Ehret, U. A decade of Predictions in Ungauged Basins (PUB)—a review. *Hydrological sciences journal*, *58*(6), 1198-1255. https://doi.org/10.1080/02626667.2013.803183, 2013.

Hu, D., Cao, S., Chen, S., Deng, L., & Feng, N. Monitoring spatial patterns and changes of surface net radiation in urban and suburban areas using satellite remote-sensing data. *International Journal of Remote Sensing*, *38*(4), 1043-1061. https://doi.org/10.1080/01431161.2016.1275875, 2017.

Huang, Yinghuai . High spatiotemporal resolution mapping of global urban change from 1985 to 2015. figshare. Dataset. https://doi.org/10.6084/m9.figshare.11513178.v1, 2020.

Immerzeel, W., and, & Droogers, P. Calibration of a distributed hydrological model based on satellite evapotranspiration. *Journal of Hydrology*, *349*(3-4), 411-424. https://doi.org/10.1016/j.jhydrol.2007.11.017, 2008.

Kauffeldt, A., Halldin, S., Rodhe, A., Xu, C.-Y., & Westerberg, I. K. Disinformative data in large-scale hydrological modelling. *Hydrology and Earth System Sciences*, *17*(7), 2845-2857. https://doi.org/10.5194/hess-17-2845-2013, 2013

Klingler, C., Schulz, K., & Herrnegger, M. LamaH-CE: LArge-SaMple DAta for Hydrology and Environmental Sciences for Central Europe. *Earth System Science Data*, *13*(9), 4529-4565. https://doi.org/10.5194/essd-13-4529-2021, 2021.

Kovács, G. Proposal to construct a coordinating matrix for comparative hydrology. *Hydrological sciences journal*, *29*(4), 435-443. https://doi.org/10.1080/02626668409490961, 1984.

Kratzert, F., Klotz, D., Shalev, G., Klambauer, G., Hochreiter, S., & Nearing, G. Benchmarking a catchment-aware long short-term memory network (LSTM) for large-scale hydrological modeling. *Hydrol. Earth Syst. Sci. Discuss*, *2019*, 1-32. https://doi.org/10.5194/hess-2019-368, 2019a.

Kratzert, F., Klotz, D., Shalev, G., Klambauer, G., Hochreiter, S., & Nearing, G. Towards learning universal, regional, and local hydrological behaviors via machine learning applied to large-sample datasets. *Hydrology and Earth System Sciences*, *23*(12), 5089-5110. https://doi.org/10.5194/hess-23-5089-2019, 2019b.

Kratzert, F., Nearing, G., Addor, N., Erickson, T., Gauch, M., Gilon, O., Gudmundsson, L., Hassidim, A., Klotz, D., & Nevo, S. Caravan-A global community dataset for large-sample hydrology. *Scientific Data*, *10*(1), 61. https://doi.org/10.1038/s41597-023-01975-w, 2023.

Lehner, B., Messager, M. L., Korver, M. C., & Linke, S. Global hydro-environmental lake characteristics at high spatial resolution. *Scientific Data*, *9*(1), 351. https://doi.org/10.1038/s41597-022-01425-z, 2022.

Li, B., Rodell, M., Kumar, S., Beaudoing, H. K., Getirana, A., Zaitchik, B. F., de Goncalves, L. G., Cossetin, C., Bhanja, S., & Mukherjee, A. Global GRACE data assimilation for groundwater and drought monitoring: Advances and challenges. *Water Resources Research*, *55*(9), 7564-

866 7586. https://doi.org/10.1029/2018WR024618, 2019.

867 Lin, P., Rajib, M. A., Yang, Z. L., Somos-Valenzuela, M., Merwade, V., Maidment, D. R., Wang, Y., &
868   Chen, L. Spatiotemporal evaluation of simulated evapotranspiration and streamflow over Texas
869   using the WRF-Hydro-RAPID modeling framework. *JAWRA Journal of the American Water*
870   *Resources Association*, *54*(1), 40-54. https://doi.org/10.1111/1752-1688.12585, 2018.

871 Lin, P. R., Pan, M., Beck, H. E., Yang, Y., Yamazaki, D., Frasson, R., David, C. H., Durand, M., Pavelsky,
872   T. M., Allen, G. H., Gleason, C. J., & Wood, E. F. Global Reconstruction of Naturalized River
873   Flows at 2.94 Million Reaches. *Water Resources Research*, *55*(8), 6499-6516.
874   https://doi.org/10.1029/2019wr025287, 2019.

875 Lin, P. R., Pan, M., Wood, E. F., Yamazaki, D., & Allen, G. H. A new vector-based global river network
876   dataset accounting for variable drainage density. *Scientific Data*, *8*(1). https://doi.org/ARTN
877   2810.1038/s41597-021-00819-9, 2021.

878 Linke, S., Lehner, B., Ouellet Dallaire, C., Ariwi, J., Grill, G., Anand, M., Beames, P., Burchard-Levine,
879   V., Maxwell, S., & Moidu, H. Global hydro-environmental sub-basin and river reach
880   characteristics at high spatial resolution. *Scientific Data*, *6*(1), 283.
881   https://doi.org/10.1038/s41597-019-0300-6, 2019.

882 Liu, X., Huang, Y., Xu, X., Li, X., Li, X., Ciais, P., Lin, P., Gong, K., Ziegler, A. D., & Chen, A. High-
883   spatiotemporal-resolution mapping of global urban change from 1985 to 2015. *Nature*
884   *Sustainability*, *3*(7), 564-570. https://doi.org/10.1038/s41893-020-0521-x, 2020.

885 Lu, J., Wang, G., Chen, T., Li, S., Hagan, D. F. T., Kattel, G., Peng, J., Jiang, T., & Su, B. A harmonized
886   global land evaporation dataset from model-based products covering 1980–2017. *Earth System*
887   *Science Data*, *13*(12), 5879-5898. https://doi.org/10.5194/essd-13-5879-2021, 2021.

888 Lucas-Borja, M. E., Carrà, B. G., Nunes, J. P., Bernard-Jannin, L., Zema, D. A., Zimbone, S. M. Impacts
889   of land-use and climate changes on surface runoff in a tropical forest watershed (Brazil),
890   Hydrological Sciences Journal, 65:11, 1956-1973, https://doi.org/10.1016/j.catena.2006.04.015,
891   2020.

892 Martens, B., Miralles, D. G., Lievens, H., Van Der Schalie, R., De Jeu, R. A., Fernández-Prieto, D., Beck,
893   H. E., Dorigo, W. A., & Verhoest, N. E. GLEAM v3: Satellite-based land evaporation and root-
894   zone soil moisture. *Geoscientific Model Development*, *10*(5), 1903-1925.
895   https://doi.org/10.5194/gmd-10-1903-2017, 2017.

896 Merchant, C. J., Paul, F., Popp, T., Ablain, M., Bontemps, S., Defourny, P., Hollmann, R., Lavergne, T.,
897   Laeng, A., & De Leeuw, G. Uncertainty information in climate data records from Earth
898   observation. *Earth System Science Data*, *9*(2), 511-527. https://doi.org/10.5194/essd-9-511-
899   2017, 2017.

900 Miralles, D. G., Holmes, T., De Jeu, R., Gash, J., Meesters, A., & Dolman, A. Global land-surface
901   evaporation estimated from satellite-based observations. *Hydrology and Earth System Sciences*,
902   *15*(2), 453-469. https://doi.org/10.5194/hess-15-453-2011, 2011.

903 Muñoz-Sabater, J., Dutra, E., Agustí-Panareda, A., Albergel, C., Arduini, G., Balsamo, G., Boussetta, S.,
904   Choulga, M., Harrigan, S., & Hersbach, H. ERA5-Land: A state-of-the-art global reanalysis
905   dataset for land applications. *Earth System Science Data*, *13*(9), 4349-4383.
906   https://doi.org/10.5194/essd-13-4349-2021, 2021.

907 Muñoz Sabater, J. ERA5-Land hourly data from 1981 to present. Copernicus Climate Change Service
908   (C3S) Climate Data Store (CDS)., https://doi.org/10.24381/cds.e2161bac, 2019.

909 Nandi, S., & Reddy, M. J. An integrated approach to streamflow estimation and flood inundation

910   mapping using VIC, RAPID and LISFLOOD-FP. *Journal of Hydrology*, *610*, 127842.
911   https://doi.org/10.1016/j.jhydrol.2022.127842, 2022.

912   Newman, A. J., Clark, M. P., Sampson, K., Wood, A., Hay, L. E., Bock, A., Viger, R. J., Blodgett, D.,
913   Brekke, L., Arnold, J. R., Hopson, T., & Duan, Q. Development of a large-sample watershed-
914   scale hydrometeorological data set for the contiguous USA: data set characteristics and
915   assessment of regional variability in hydrologic model performance. *Hydrology and Earth*
916   *System Sciences*, *19*(1), 209-223. https://doi.org/10.5194/hess-19-209-2015, 2015

917   Niraula, R., Meixner, T., & Norman, L. M. Determining the importance of model calibration for
918   forecasting absolute/relative changes in streamflow from LULC and climate changes. *Journal*
919   *of Hydrology*, *522*, 439-451. https://doi.org/10.1016/j.jhydrol.2015.01.007, 2015.

920   Qu, S., Wang, L., Lin, A., Zhu, H., & Yuan, M. What drives the vegetation restoration in Yangtze River
921   basin, China: climate change or anthropogenic factors? *Ecological Indicators*, *90*, 438-450.
922   https://doi.org/10.1016/j.ecolind.2018.03.029, 2018.

923   Razavi, T., & Coulibaly, P. Streamflow prediction in ungauged basins: review of regionalization methods.
924   *Journal of hydrologic engineering*, *18*(8), 958-975. https://doi.org/10.1061/(ASCE)HE.1943-
925   5584.0000690, 2013

926   Ren, K., Fang, W., Qu, J., Zhang, X., & Shi, X. Comparison of eight filter-based feature selection
927   methods for monthly streamflow forecasting–three case studies on CAMELS data sets. *Journal*
928   *of Hydrology*, *586*, 124897. https://doi.org/10.1016/j.jhydrol.2020.124897, 2020.

929   Riggs, R. M., Allen, G. H., Wang, J., Pavelsky, T. M., Gleason, C. J., David, C. H., & Durand, M.
930   Extending global river gauge records using satellite observations. *Environmental Research*
931   *Letters*. https://doi.org/10.1088/1748-9326/acd407, 2023.

932   Schaake, J, Cong, S, and Duan, Q. 2006. "U.S. MOPEX DATA SET". United States.
933   https://www.osti.gov/servlets/purl/899413.Schmidt, A. H., Montgomery, D. R., Huntington, K.
934   W., & Liang, C. The question of communist land degradation: new evidence from local erosion
935   and basin-wide sediment yield in Southwest China and Southeast Tibet. *Annals of the*
936   *Association of American Geographers, 101*(3), 477-496.
937   https://doi.org/10.1080/00045608.2011.560059, 2011.

938   Schreiner-McGraw, A. P., & Ajami, H. Impact of uncertainty in precipitation forcing data sets on the
939   hydrologic budget of an integrated hydrologic model in mountainous terrain. *Water Resources*
940   *Research*, *56*(12), e2020WR027639. https://doi.org/10.1029/2020WR027639, 2020.

941   Singer, M. B., Asfaw, D. T., Rosolem, R., Cuthbert, M. O., Miralles, D. G., MacLeod, D., Quichimbo, E.
942   A., & Michaelides, K. Hourly potential evapotranspiration at 0.1 resolution for the global land
943   surface from 1981-present. *Scientific Data*, *8*(1), 224. https://doi.org/10.1038/s41597-021-
944   01003-9, 2021.

945   Sörensson, A. A., & Ruscica, R. C. Intercomparison and uncertainty assessment of nine
946   evapotranspiration estimates over South America. *Water Resources Research*, *54*(4), 2891-2908.
947   https://doi.org/10.1002/2017WR021682, 2018.

948   Tang, G., Clark, M. P., & Papalexiou, S. M. EM-Earth: The ensemble meteorological dataset for planet
949   Earth. *Bulletin of the American Meteorological Society*, *103*(4), E996-E1018.
950   https://doi.org/10.1175/BAMS-D-21-0106.1, 2022.

951   Tang, G., Clark, M., Papalexiou, S. EM-Earth: The Ensemble Meteorological Dataset for Planet Earth.
952   Federated Research Data Repository. https://doi.org/10.20383/102.0547, 2022.

953   Tang, G., Clark, M. P., Knoben, W. J. M., Liu, H., Gharari, S., Arnal, L., et al. The impact of

meteorological forcing uncertainty on hydrological modeling: A global analysis of cryosphere basins. *Water Resources Research, 59,* e2022WR033767. https://doi.org/10.1029/2022WR0337, 2023.

Thackeray, C. W., Hall, A., Norris, J., & Chen, D. Constraining the increased frequency of global precipitation extremes under warming. *Nature Climate Change*, *12*(5), 441-448. https://doi.org/10.1038/s41558-022-01329-1, 2022.

Ukhurebor, K. E., Azi, S. O., Aigbe, U. O., Onyancha, R. B., & Emegha, J. O. Analyzing the uncertainties between reanalysis meteorological data and ground measured meteorological data. *Measurement*, *165*, 108110. https://doi.org/10.1016/j.measurement.2020.108110, 2020.

Velpuri, N. M., and G. B. Senay. "Analysis of long-term trends (1950–2009) in precipitation, runoff and runoff coefficient in major urban watersheds in the United States." Environmental Research Letters 8, no. 2 , 024020. https://doi.org/10.1088/1748-9326/8/2/024020, 2013.

Vermote, Eric; NOAA CDR Program. NOAA Climate Data Record (CDR) of AVHRR Leaf Area Index (LAI) and Fraction of Absorbed Photosynthetically Active Radiation (FAPAR), Version 5. [LAI]. NOAA National Centers for Environmental Information. https://doi.org/10.7289/V5TT4P69., 2019.

Wang, J., Walter, B. A., Yao, F., Song, C., Ding, M., Maroof, A. S., Zhu, J., Fan, C., McAlister, J. M., & Sikder, S. GeoDAR: georeferenced global dams and reservoirs dataset for bridging attributes and geolocations. *Earth System Science Data*, *14*(4), 1869-1899. https://doi.org/10.5194/essd-14-1869-2022, 2022.

Wilby, R. L., & Dessai, S. Robust adaptation to climate change. *Weather*, 65(7), 180–185. https://doi.org/10.1002/wea.543, 2010

Xiong, J., Yin, J., Guo, S., He, S., & Chen, J. Annual runoff coefficient variation in a changing environment: A global perspective. *Environmental Research Letters*, *17*(6), 064006. https://doi.org/10.1088/1748-9326/ac62ad, 2022.

Yamazaki, D., Ikeshima, D., Sosa, J., Bates, P. D., Allen, G. H., & Pavelsky, T. M. MERIT Hydro: a high-resolution global hydrography map based on latest topography dataset. *Water Resources Research*, *55*(6), 5053-5073. https://doi.org/10.1029/2019WR024873, 2019.

Yamazaki, D., Ikeshima, D., Tawatari, R., Yamaguchi, T., O'Loughlin, F., Neal, J. C., Sampson, C. C., Kanae, S., & Bates, P. D. A high-accuracy map of global terrain elevations. *Geophysical Research Letters*, *44*(11), 5844-5853. https://doi.org/10.1002/2017GL072874, 2017.

Yang, L., Yang, Y., Villarini, G., Li, X., Hu, H., Wang, L., Blöschl, G., & Tian, F. Climate more important for Chinese flood changes than reservoirs and land use. *Geophysical Research Letters*, *48*(11), e2021GL093061. https://doi.org/10.1029/2021GL093061, 2021.

Yin, Z., Lin, P., Riggs, R., Allen, G. H., Lei, X., Zheng, Z., & Cai, S. A Synthesis of Global Streamflow characteristics, Hydrometeorology, and catchment Attributes (GSHA) for Large Sample River-Centric Studies V1.1 (1.0) [Data set]. Zenodo. https://doi.org/10.5281/zenodo.8090704, 2023.

Ziyun Yin, Peirong Lin, Ryan Riggs, George H. Allen, Xiangyong Lei, Ziyan Zheng, & Siyu Cai. A Synthesis of Global Streamflow characteristics, Hydrometeorology, and catchment Attributes (GSHA) for Large Sample River-Centric Studies V1.1 (1.3) [Data set]. Zenodo. https://doi.org/10.5281/zenodo.10127757, 2023.

Zaitchik, B. F., Rodell, M., & Reichle, R. H. Assimilation of GRACE terrestrial water storage data into a land surface model: Results for the Mississippi River basin. *Journal of Hydrometeorology*, *9*(3), 535-548. https://doi.org/10.1175/2007jhm951.1, 2008.

Zhang, J., Lin, P., Gao, S., & Fang, Z. Understanding the re-infiltration process to simulating streamflow in North Central Texas using the WRF-hydro modeling system. *Journal of Hydrology*, *587*, 124902. https://doi.org/10.1016/j.jhydrol.2020.124902, 2020.

Zhang, J., Wang, T., & Ge, J. Assessing vegetation cover dynamics induced by policy-driven ecological restoration and implication to soil erosion in southern China. *PLoS One*, *10*(6), e0131352. https://doi.org/10.1371/journal.pone.0131352, 2015.

Zhang, S., Zhou, L., Zhang, L., Yang, Y., Wei, Z., Zhou, S., Yang, D., Yang, X., Wu, X., & Zhang, Y. Reconciling disagreement on global river flood changes in a warming climate. *Nature Climate Change*, 1-8. https://doi.org/10.1038/s41558-022-01539-7, 2022.

Zhang, Y., & Liang, S. Changes in forest biomass and linkage to climate and forest disturbances over Northeastern China. *Global change biology*, *20*(8), 2596-2606. https://doi.org/10.1111/gcb.12588, 2014.

Zhang, Y., Zheng, H., Zhang, X., Leung, L. R., Liu, C., Zheng, C., Guo, Y., Chiew, F. H., Post, D., & Kong, D. Future global streamflow declines are probably more severe than previously estimated. *Nature Water*, 1-11. https://doi.org/10.1038/s44221-023-00030-7, 2023.